Setup of a low Temperature Silicon Detector for the COMPASS Experiment

Diploma Thesis
by
Anna-Maria Elisabeth Fuchs

Physics Department E18
Technical University of Munich
December 2003

Setup of a low Temperature Silicon Detector for the COMPASS Experiment

Diploma Thesis

by

Anna-Maria Elisabeth Fuchs

Physics Department E18

Technical University of Munich

December 2003

Abstract

The COMPASS experiment at CERN investigates the structure of the nucleon with both muon and hadron beams of high intensity. Double-sided silicon microstrip detectors are are used for beam definition and track reconstruction with high spatial resolution in the target region.
The radiation damage caused especially by the hadron beam is so large that the silicon detectors show a noticeable degradation of their performance already after one beamtime. Therefore, they are operated at cryogenic temperature of 130 K to exploit the so-called Lazarus effect. Thus, their lifetime can be extended by a factor of 5.
The first part of this thesis deals with the construction of the liquid nitrogen cooled silicon detector. Especially the development of a low mass, vacuum and light tight detector window is discussed in detail.
The second part reports about the commissioning of the silicon detector and first results of the performance tests during the 2003 beamtime. The main focus of the analysis is to determine the spatial resolution, efficiency and time resolution of a double sided silicon detector in warm and cryogenic operation.

Contents

List of Figures

Chapter 1

Introduction

The COMPASS experiment at CERN is a fixed target experiment. High statistics and a wide momentum range are needed to investigate the structure and spectroscopy on the nucleon with both muon and hadron beams. Chapter 2 will give a short introduction in the experiment and its variety of physics which can be analyzed.

Silicon microstrip detectors have an excellent spatial resolution with a high-rate capability which makes them uniquely suitable for beam definition especially in very high intensity particle beams as used in the COMPASSexperiment. A special feature of the silicon detectors in COMPASS is their double sided readout. A short review about the basic physical principles of a silicon detector in general and the hardware setup of the COMPASS silicon trackers is given in chapter 3.

The damage caused by the hadron beam is so high that the detectors show a noticeable degradation of their performance already after one beamtime. The Lazarus effect is an experimentally observed effect [Pal98] by the RD39 collaboration at CERN, that the charge collection efficiency (CCE) of a radiation damaged silicon detector recovers if the detector is operated at cryogenic temperatures. The maximum increase of the CCE is predicted at a temperature of 130 K. To be prepared for the hadron beam and taking advantage of the Lazarus effect, a silicon station for cryogenic operation was developed as an advancement of the already existing detector setup. The main modifications of the setup are mentioned in chapter 4. Within the scope of this thesis a low mass, vacuum and light tight detector window was designed and tested.

For the beamtime 2003 three silicon stations were installed in the COMPASS experiment for warm operation. The commissioning of the cryogenic silicon detector and first results of the performance tests during the 2003 beamtime are presented in chapter 5. The main focus of the detector analysis is the extraction of the spatial resolution which is challenging since the silicon detectors have the best spatial resolution of all COMPASS detectors. Further topics are the comparison between the performance of warm and cryogenic operated silicon detectors concentrated on selected detector properties.

Chapter 2

The COMPASS Experiment

The **Co**mmon **M**uon and **P**roton **A**pparatus for **S**tructure and **S**pectroscopy is a high-luminosity fixed target experiment at the Super Proton Synchrotron (SPS) at CERN[1]. COMPASS is designed to be a multipurpose experiment consisting of two physics programs with muons and hadrons. Its aim is to investigate spin structure functions as well as many properties of hadronic systems. The beam particles are produced in a conversion target using the 400 GeV protons of the SPS. The commissioning of the spectrometer was done in the year 2001 and first physics data with a 160 GeV muon beam were taken in 2002 and 2003.

2.1 The M2 Beam Line

The COMPASS experiment is provided with CERN's tertiary high-intensity muon beam of the beam line M2. The SPS accelerates protons or heavy ions. If other particles for an experiment are needed a production target has to be inserted. In this case of COMPASS the primary SPS protons hit the T6 production target and secondary beam particles are produced. It depends on the polarity of the bending magnets whether pions, protons or kaons as secondary particles are following the transfer line.

After the production target there is an approximately 600 meters long decay section where the produced secondary hadrons decay, e.g. the π^- into μ^- and an anti-neutrino. For muons the pion and kaon decay channel is used. At the end of this section the remaining hadrons are stopped by a 9.9 m thick Beryllium hadron absorber.

[1] **C**onseil **E**uropéenne pour la **R**echerche **N**ucléaire

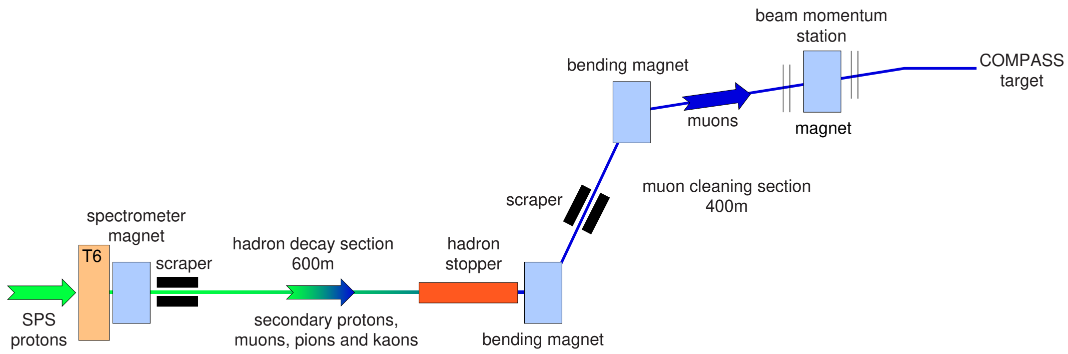

Figure 2.1: A schematic view of the M2 beam line [Nie00]

The generated muons are extracted by bending magnets and pass a muon cleaning section of 400 m before they reach the COMPASS experimental area. To purify the muon beam, a heavy concrete absorber is placed before the experiment. The muons are passing this block with only little energy loss, while hadrons and electrons are stopped by creating hadronic or electromagnetic showers. The momentum of the beam particles is measured with the beam momentum station at the last bending magnet in front of the experimental area. The mean life of the pion beam is coming up to 8 km, that means the intensity of the hadron beam is much higher with the same energy.

The spot size for the muon beam is typically $7 \times 8\,\mathrm{mm}^2$ RMS in the horizontal and vertical plane with a divergence of less than 0.5 mrad $\times$ 1 mrad. The flux of the beam is up to $2 \cdot 10^8$ muons per SPS cycle [Gat00, Gat01] and the momentum range is between 60 to 190 GeV$/c$. There are also two additional beams available, a secondary hadron beam (momentum range 40 to 280 GeV$/c$, maximum flux of $2 \cdot 10^8$ hadrons per spill[2] with a spot size down to $1.1 \times 1.5\,\mathrm{mm}^2$ RMS) as well as a low intensity calibration electron beam (momentum range up to 60 GeV$/c$ and typical flux of $10^3 - 10^4$ per spill).

2.2 The COMPASS Detector

The COMPASS experiment consists of a high rate, two-stage magnetic spectrometer. Its key features are high statistics and high precision. High statistics is reached reached with a high intensity beam with beam particles in the order of 10^8 particles per SPS spill and high trigger rates. The precision is achieved with a two stage spectrometer equipped with tracking and particle identification detectors, magnets (bending power 1.0 Tm and 1.5 Tm), hadronic and electromagnetic

[2]spill: particle extraction during one SPS cycle

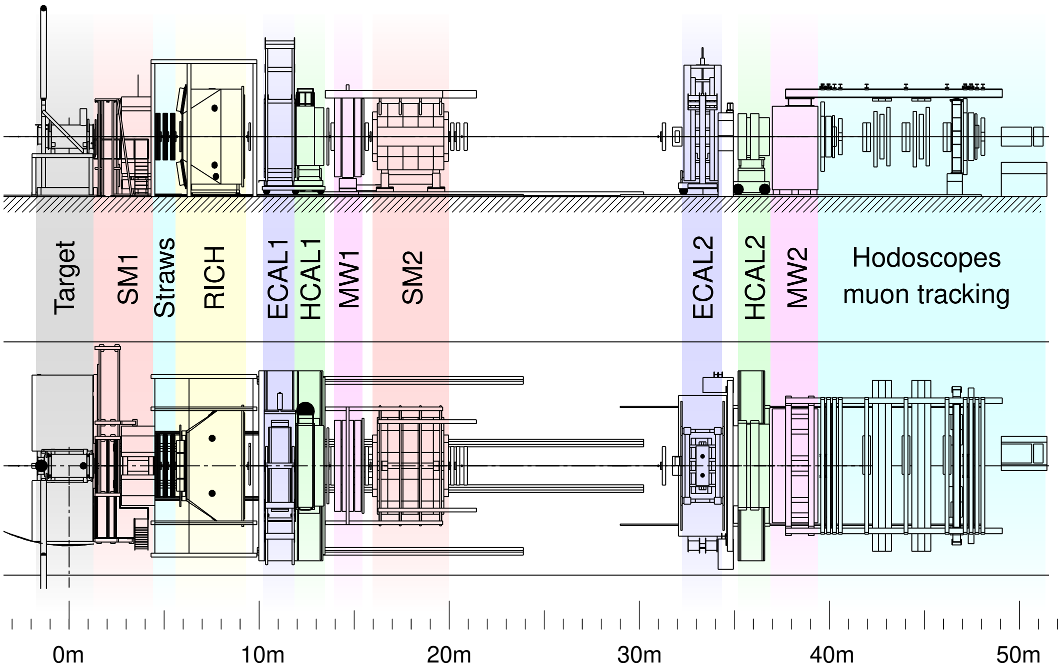

Figure 2.2: Top and side view of the COMPASS spectrometer [Gru01]

calorimeters and muon detection systems. These two stages are two independent spectrometers. The first stage has acceptance for low momentum particles with large deflections (±180 mrad) and the second stage for high momentum particles (±25 mrad). The angular resolution is in the size down to 10 μrad for small scattering angles and a lateral resolution down to 7 μm can be reached. The dynamical range which can be analyzed is up to 150 GeV.

Upstream of the target, tracking detectors are needed for beam definition. Silicon microstrip trackers are very suitable for this purpose because of their high spatial resolution of better than 15 μm. Also scintillating fibers are used, because of their precise time resolution of $\sim$ 400 ps.

In general the tracking system of COMPASS consists of **L**arge **A**rea **T**rackers (**LAT**) covering the outer region with lowest track density and **S**mall **A**rea **T**rackers (**SAT**) used for the inner region including the beam. Other SATs are the for COMPASS new developed Gas Electron Multipliers (GEMs) and Micromesh Gaseous Detectors (Micromegas). The Straw Chambers, Multi Wire Proportional Counters (MWPCs), Drift Chambers (DC) and Multi Wire chambers (MW45) are COMPASS slarge area trackers. The calorimetry in COMPASS is taken on hadronic and electromagnetic calorimeters from which high spatial and energy resolution is required.
For particle identification a Ring Imaging Cherenkov Detector (RICH) was built. For the muon program a polarized Deuterium target is used to measure spin de-

pendent observables. For the hadron setup, different target materials like copper and lead in combination with a silicon beam telescope before and after the target will be used. In figure 2.2 the schematic draft of the top and side view of the COMPASS spectrometer is shown.

2.3 The COMPASS Physics Program

The COMPASS experiment is investigating muon and hadron physics. A detailed description about the COMPASS physic programs is given in [CO96].

Muon Program During the muon beam a rich spin physics program will be analyzed. The measurement of the gluon polarization $\Delta G/G$ is a main goal of the COMPASS experiment since preceding experiments like SMC[3] indicated that the spin content of the nucleon is not only given by the spin of the valence quark. The gluon helicity distribution $\Delta G(x)$ will be measured using deep inelastic scattering of a polarized muon beam of 100-190 GeV off a polarized target and studying the longitudinal spin asymmetry of open charm leptoproduction. Another aim is the measurement of Λ and $\bar{\Lambda}$ polarization as well as transverse and longitudinal spin distribution functions.

Hadron Program Charm physics allows to study the influence of strong interactions on the weak decay of hadrons at a scale where QCD predictions are already possible. Up to now there is not much known about the properties of charmed baryons. There are still $1/2^{+}$ ground states which should be observed. Lifetimes of charmed baryons, non-leptonic decays and semileptonic decays will be studied to increase the knowledge about charmed baryons. Also for charmed D mesons the leptonic decays will be studied.

QCD predicts constructions of bound states with valence gluons (*hybrids*) or bound states consisting only of gluons (*glueballs*) since gluons carry color charge. COMPASS with its high statistics should also be able to see five-quark systems and other exotic combinations if only their binding energy is high enough for a bound state.

With Primakoff scattering many different reactions can be studied, e.g. the distribution of quark configurations in hadronic matter and hadron polarizabilities. The Primakoff mechanism is Compton scattering with virtual photons in inverse kinematics. COMPASS is going to analyze it with a kaon, π and Σ beam.

[3] **S**pin **M**uon **C**ollaboration Experiment at CERN

Chapter 3

Silicon Microstrip Detectors in COMPASS

Silicon microstrip detectors have an excellent spatial resolution in combination with a high-rate capability which makes them uniquely suitable for beam definition especially in very high intensity particle beams as used in the COMPASS experiment. In this chapter the main operation principles of a silicon detector are explained. The problem of radiation damage and possible solutions are discussed as well. In the second part of the chapter there is a short overview about the silicon microstrip detector developed for the COMPASS experiment.

3.1 Basic Operation Principles

3.1.1 Silicon Properties

A charged particle which is crossing the silicon detector loses at least 3.6 eV creating an electron-hole pairs. Due to the high density of the silicon, the range of energetic secondary electrons is reduced whereby a good spatial resolution is achieved. The collected signal is a function of the detector thickness. To minimize multiple Coulomb scattering the detector thickness has to be as low as possible. The signal to noise ratio gives a lower bound for the detector thickness. A good compromise are, silicon detectors with 300 μm thickness. The typical signal of $3.2 \cdot 10^4$ electron-hole pairs can be observed with low noise electronics. This background noise comes from intrinsic carriers which are electron hole pairs constantly generated by thermal excitation. Together with recombination there is always a equilibrium concentration of electron-hole pairs in intrinsic material.

Often the silicon material is doped with penta- or trivalent-atoms, called impurities, to alter the semiconductor's properties. A material is called n-type if the impurity atoms have five valence electrons. The fifth electron is called excess electron and creates donor impurity levels in the energy gap, which lies close to the valence band. A part from that p-type material is doped with atoms which has three valence electrons.

The excess electrons are easily lifted in the conduction band at room temperature, which is enhancing the conductivity of the semiconductor. In n-type material the electrons are called majority carriers because the current arises mainly from their movement, in p-type material the holes are the majority carriers. The holes are named minority carriers. The product of the electron and hole concentration n and p is

$$np = n_i^2 = AT^3 e^{-\frac{E_g}{kT}}, \tag{3.1}$$

where E_g is the gap energy (1.11 eV in silicon), n_i the intrinsic carrier density, k the Boltzmann constant, T the temperature and A is a temperature independent constant.

The intrinsic charge carrier density is four orders of magnitude higher than expected signal [Pei92] and the signal to noise ratio in doped material would be even worse. One possibility to increase the signal to noise ratio is to cool the crystal. The other way is to operate the detector with a bias voltage and deplete the crystal of its charge carriers so that it behaves like a resistor. This is realized with a reverse biased pn-junction.

3.1.2 Mobility

With an external applied electric field the drift velocity of the electrons v_e and the holes v_h in the silicon can be written as

$$v_e = \mu_e E, \quad v_h = \mu_h E. \tag{3.2}$$

E is the magnitude of the electrical field, μ_e and μ_h are the mobilities of the electrons and the holes. The mobility describes how easy the charge carrier can drift in an electrical field. It is also temperature dependent. In the range between $100 - 400$ K the dependency between mobility and temperature T is given by

$$\mu \propto T^{-m}. \tag{3.3}$$

The exponent m depends on the type of material and on the charge carrier and is 2.5 for electrons, and 2.7 for holes in silicon [Leo94]. The mobility also determines the current in the semiconductor. For holes the mobility is 480 $\mathrm{cm}^2/\,\mathrm{Vs}$ and 1350 $\mathrm{cm}^2/\,\mathrm{Vs}$ for electrons. The resistivity ρ of the doped semiconductor, where the concentrations of acceptor impurities is much smaller than the concentration of the donor impurities, is given by

$$\rho = \frac{1}{q\mu N_d}, \tag{3.4}$$

with the electron charge q, the donors concentration N_d and mobility μ. Due to the temperature dependency of the mobility also the resistivity depends on the temperature. It is decreasing at lower temperatures.

3.1.3 pn Junction

At the junction of p- and n-type material there is a gradient of the free charge carrier density. The majority carriers of each material type diffuse across the junction. Holes in the p-type material diffuse towards the n-region and recombine with electrons. Electrons from the n-side are filling up holes in the p-region.

This creates a region around the junction with net positive and negative charge of the immobile unneutralized acceptor and donor ions. This region is called space charge or depletion zone, see figure 3.1. But the whole pn-junction is neutral. This "built-in" potential leads to an barrier so that no further migration is possible and the system comes to an equilibrium. In the depletion zone there are no free charge carriers any longer.

Usually the silicon tracking detectors are operated in reversed bias. Without reversed bias the intrinsic field on the junction is not intense enough to provide an efficient charge collection and an increase of the thickness of the depletion zone. At a reverse bias junction a negative voltage is applied on the p-side. That means the holes e.g. are attracted away from the junction in the p-region to the p-contact. This is analogue for the electrons in the n-side. The net effect is an enlargement of the depletion zone and thus of the sensitive volume for radiation detection. The maximum bias voltage is given by the resistance of the semiconductor. The higher the resistance, the more convenient it is if the silicon detector is used for tracking.

The difference of the mobility of electrons and holes yields a larger depletion depth of the material in the n-type compared to p-type silicon. For a particle detector it is convenient to have a p^+n junction, i.e. a high concentration of acceptor

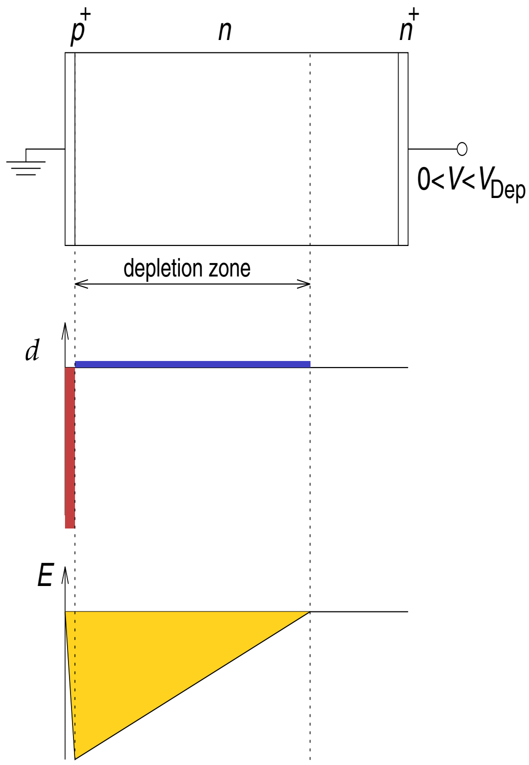

Figure 3.1: A double-sided silicon detector with pn junction; it is shown the geometry, the charge density and the electric field distribution in the depletion zone [Wag01]

(p^+) and a low concentration of donor atoms. A 300 μm thick n-type silicon layer serves as an active volume for the detector and a 0.4 μm layer of p-type material is just necessary to deplete it of free carriers. If one impurity concentration is much larger than the other, the width W of the depleted region can be calculated by

$$W = \sqrt{2\epsilon(V_{\text{bias}} + V_{bi})/Ne} = \sqrt{2\rho\mu\epsilon(V_{\text{bias}} + V_{bi})}, \tag{3.5}$$

with external bias voltage V, the "built-in" voltage V_{bi}, doping concentration N, electronic charge e, dielectric constant ϵ, the resistivity ρ and charge carrier mobility μ, [PDG00].

3.1.4 Leakage Current

A depleted region is free of majority charge carriers. But electron-hole pairs are generated continually everywhere within the volume of the crystal. Due to the electric field of the bias voltage these created carriers are separated and cannot recombine. This can be measured as the generation cuFirst I would like to thank Prof. Stephan Paul for giving me the chance to work on the cryogenic setup for a cooled silicon station and to learn how much work is necessary and how many

details have to be considered to get a low temperature detector running. Apart from that the several trips to CERN gave insight in the fascinating world of high energy particle physics.

I am deeply grateful to Jan Friedrich, for a lot of support, ideas concerning the development of the detector window and the introduction in the detector analysis. He showed a lot of patience in teaching me C++ and how to work with ROOT. I really learned a lot from him and without his continuous advice this thesis would not have been possible.

Special thanks to Rita de Masi for the introduction in cryogenic operated silicon station and for the effective installation times at CERN.

Also Boris Grube deserves many thanks for his kind help by all kinds of computer problems and Roland Kuhn as well, especially for for writing some scripts and allowing me to use his TEX style file.

Further I am much obliged to the whole COMPASS group of their support and help, I really enjoyed to be a member of them.

Thanks to Jan, Boris, Elke, Matthias, Horst and Rita for proof-reading this manuscript and for figuring out the most important bugs.rrent j_{gen}:

$$j_{\text{gen}} = \frac{1}{2} q \frac{n_i}{\tau_0} W \tag{3.6}$$

Here τ_0 is the effective lifetime of minority carriers, q the charge and $W \sim \sqrt{V_{\text{bias}}}$ the width of the depletion zone in the silicon bulk. The intrinsic carrier density $n_{\text{i}} \sim \exp\left(-\frac{E_{\text{gap}}}{kT}\right)$ is temperature dependent, the higher the temperature the higher the leakage current [Pei92]. For a fully depleted silicon detector the measured leakage current is equal to the generation current. The leakage current increases linearly with $\sqrt{V}$ until the detector is fully depleted. In reality the leakage current is the generation current plus the current which is drawing the frontend electronics.

3.1.5 Particle Detection

Particle detection is a common application of silicon detectors. The silicon wafer is equipped with readout strips which are specially doped to become n^+ and p^+ strips. The signal shape is Landau distributed and the asymmetry of this distribution is due to high energy electrons. In general the energy loss is dependent on the velocity and charge of the particle. These dependencies are well described by the Bethe Bloch formula. In a 300 μm thick silicon detector the most probable charge deposition for minimum ionizing particles is about 22000 electrons but the average charge deposition is about 32000 electrons.

A very important property is the charge collection efficiency (CCE) which describes ratio of the collected charge versus the originally generated charge. In fully depleted detectors the charge collection efficiency saturates.

A crossing particle creates a 1 μm tube of electron hole pairs through the silicon detector. Due to the electric field of the bias voltage the charge starts to drift. The electrons and holes diffuse by multiple collisions and this distribution can be described by

$$\frac{dN}{N} = \frac{1}{\sqrt{4\pi Dt}} \cdot e^{-\frac{x^2}{4Dt}} dx. \tag{3.7}$$

The fraction of the charge dN/N found in an element dx from the origin after a time t with the diffusion coefficient

$$D = \frac{kT}{q} \cdot \mu \tag{3.8}$$

is related to the mobility μ. The root mean square is

$$\sigma = \sqrt{2Dt}, \tag{3.9}$$

in addition t is inversely proportional to the mobility [Pei92].

3.2 Radiation Damages and Lazarus Effect

There are two basic mechanisms for the generation of radiation damage, bulk damage due to displacement of atoms from their lattice sites and surface damage due to charge built-in surface layers, which leads to increased surface leakage currents.

A bulk damage in the silicon is mainly caused by hadrons, high energy leptons or gammas due to displacing a Primary Knock on Atom (PKA) out of its lattice site. The energy threshold of such point defect is approximately 25 eV. The PKAs can also agglomerate to clusters for which a creating particle has to have more than about 8 MeV. The clusters and PKAs have strong effects on the detector performance depending on their concentration, energy level and electron-hole capture. Defects with deep energy levels in the middle of the gap can act as recombination or generation centers which are responsible for the increase of the reverse bias current. The effective doping concentration changes by formation of complex defects and generating charged centers after the removal of dopants. These defects brings about a change in the needed operation voltage to fully deplete the silicon

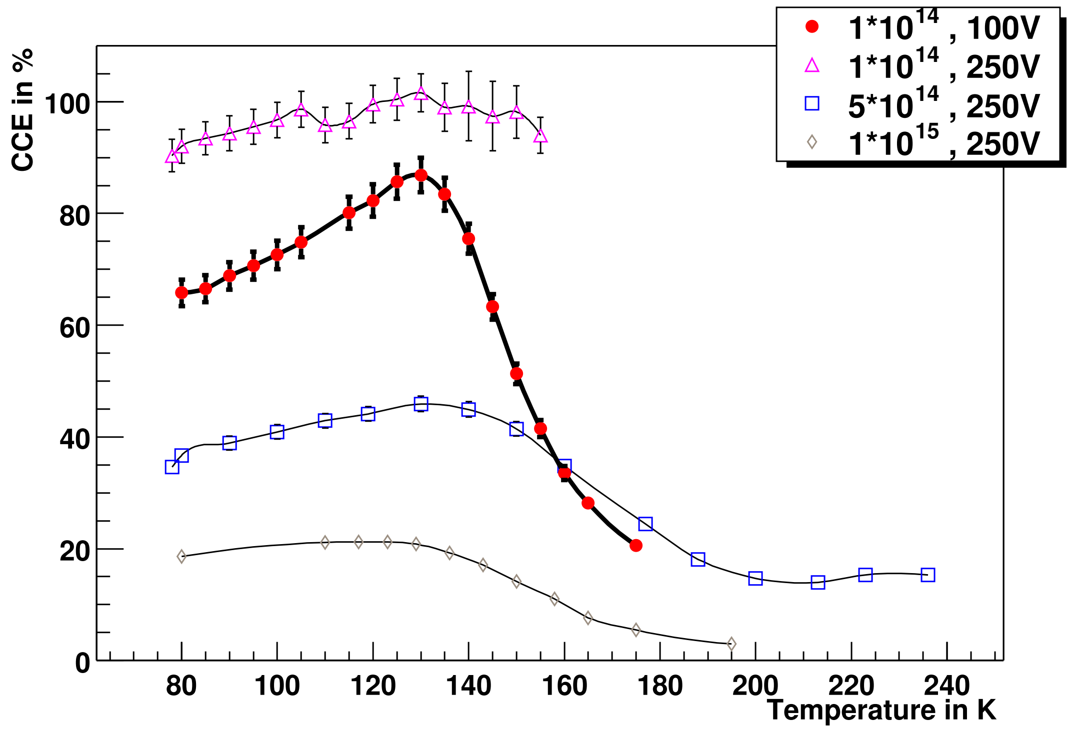

Figure 3.2: CCE dependence on the temperature: The different curves show the CCE for different radiation damage and different bias voltages [Bor00].

detector. In addition these defects could act as trapping centers which leads to a reduction of the CCE. A very detailed discussion about radiation damages on silicon particle detectors is given in [Mol99].

For radiation damaged silicon detectors two major effects can be observed, the increase of the leakage current and depletion voltages. This leads to a reduction of the CCE. The charge created by beam particles can get lost due to deep levels traps created by radiation during the charge collection time and the partial depletion of the detector in the case of high resistivity bulk, where the non-depleted part of the detector thickness (neutral base region) acts as a capacitive divider. The trapping time of these new deep levels is dominated by thermal excitation, and it is longer than for normal donor and acceptor levels. Part of the signal charge is delayed and the CCE decreases. For an irradiated detector which is not any longer usable at room temperature, the recovery of the CCE in a cooled environment was experimentally observed by RD39 collaboration. A maximum value of the recovery of the CCE at 130 K was named Lazarus effect. In figure 3.2 is shown the CCE dependence on temperature measured for different bias voltages and different radiation damages.

The current understanding of the Lazarus effect is described in [RD302]. Simpli-

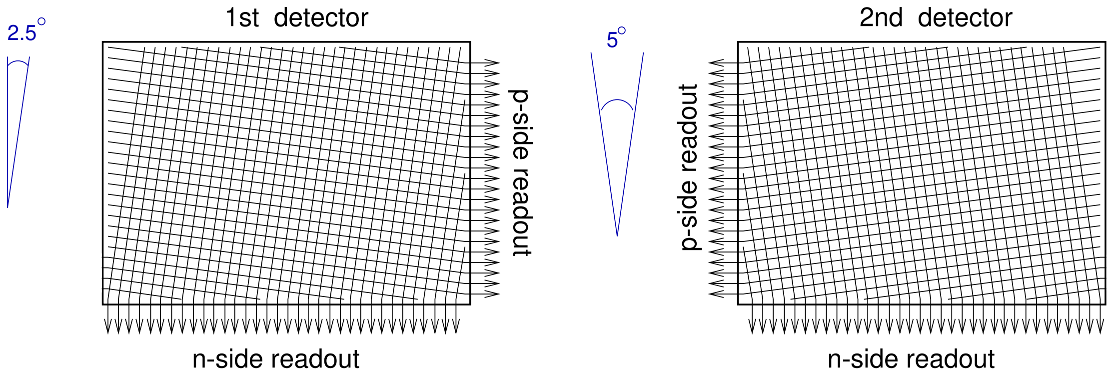

Figure 3.3: Silicon wafer layout [Abt99]

fied it can be explained that the concentrations of the charged fractions of deep levels decrease rapidly with decreasing temperature and neutral fractions dominate the trapping. But at the same time with lower temperature the intrinsic carrier density is getting smaller which means an recovery of the CCE. The product of both effects leads to an CCE-maximum of irradiated silicon at 130 K.

3.3 Detector Design

COMPASS uses silicon microstrip detectors that, were developed for HERA-B by the Semiconductor Laboratory (HLL) of the Max-Planck-Institutes in Munich and produced by SINTEF (Oslo, Norway).

The COMPASS silicon microstrip detector consists of a 280 μm thick n-type silicon bulk with $(2-3)$ kΩ cm resistivity. The active area of the silicon wafer is 50 mm × 70 mm and equipped with a fine read out pitch of 54.6 μm on the n-side and 51.7 μm on the p-side respectively. Intermediate strips on the p-side improve the spatial resolution due to charge division readout. A special feature of these silicon detectors are their double-sided readout.

Is necessary to have three or more independent projections for standalone track finding. The angle between the readout strips and the edge of the silicon wafer is 2.5°, see figure 3.3. If two silicon wafers are mounted back to back four views or readout projections respectively with a stereo angle of 5° can be achieved. One silicon station in COMPASS consists of two of these silicon microstrip detectors mounted back to back on a precision construction in a box of stainless steel (cryostat) covered with two special low mass detector windows. A detailed description about the whole silicon setup is given in [Wie03].

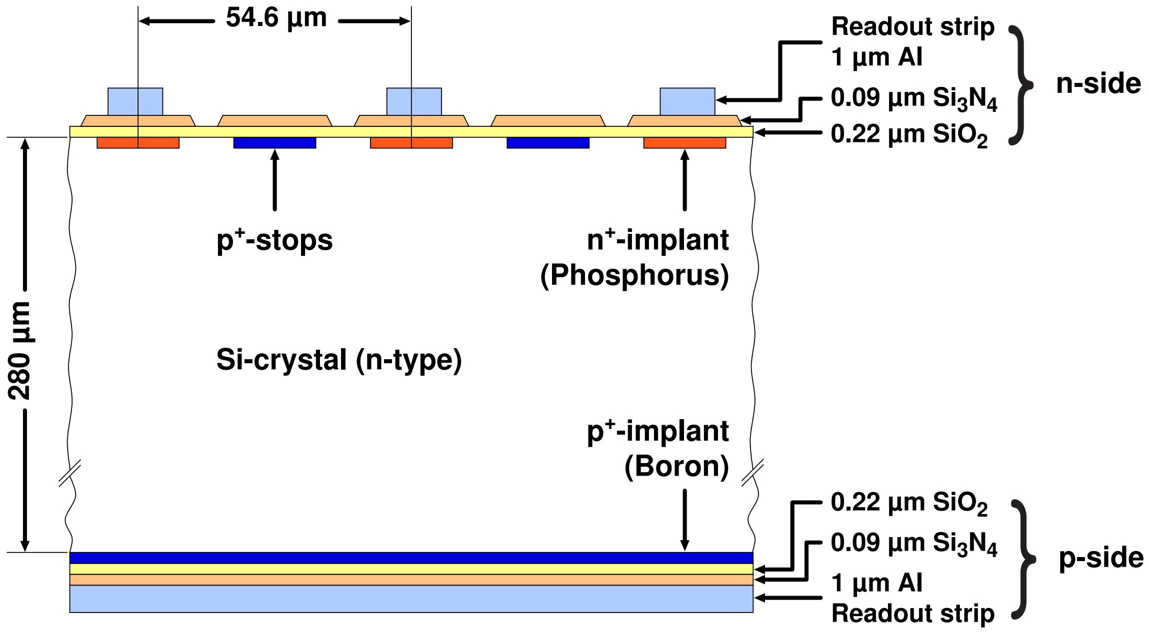

Figure 3.4: A schematic cut view of the SINTEF silicon microstrip detector [Wag01]

3.3.1 Radiation Hard Design

For COMPASS silicon detectors, developed for HERA-B experiment, was chosen due to the radiation hard design. The COMPASS silicon detectors have to cope with fluences in an hadron beam up to $6 \cdot 10^{14} / \mathrm{cm}^2$ per year of run time and the beam passing right through the center of the detector area. The HLL developed a special radiation hard design of the silicon wafer. It includes a multi guard-ring structure, a p-stop implant as separation method on the n-side as well as polysilicon resistors for strip biasing and capacitive coupling.

Radiation damage leads to very large leakage currents which can be dammed up with capacitive coupling. The readout strips consist of 1 µm thick aluminum lines which are separated from the implanted strips by a 220 nm thick layer of silicon dioxide and a 90 nm thick layer of silicon nitride. A schematic cut view can be seen in figure 3.4.

Originally punch-through contacts to the readout strips were used to bias the silicon detector. But irradiation studies [Abt99] showed that for a flux of MIPs like it is expected in COMPASS the noise per channel increases very much with this technology due to traps created in the punch-through channels. Therefore polysilicon resistors of approximately 1 MΩ respectively 10 kΩ/strip were implemented.

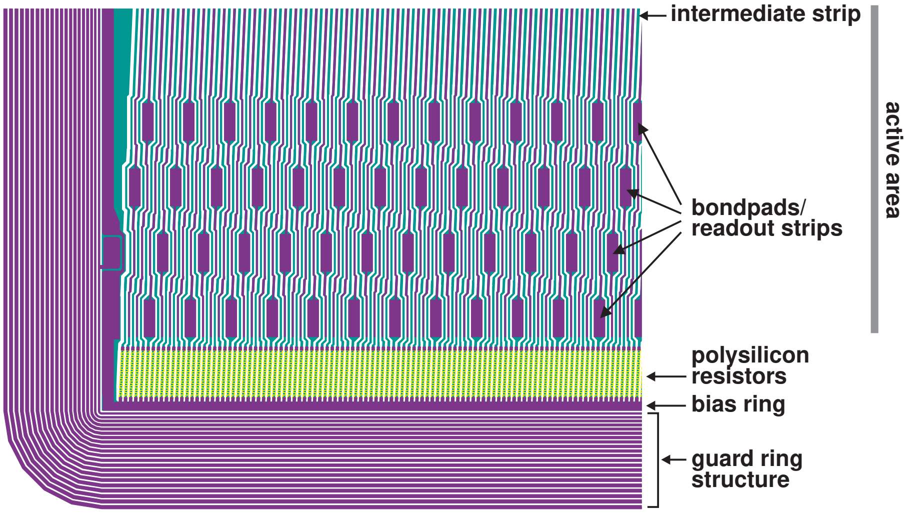

Figure 3.5: Layout of one corner of the n-side of the silicon wafer [Abt99]

Because of the radiation damage due to high particle fluences the bias voltage has to be increased by-and-by. For the SINTEF silicon wafer it was foreseen to operate up to 300 to 500 V in comparison with the nominal voltage of 60 to 100 V. The silicon wafers have to be protected by a multi guard-ring structure. This structure consists of up to 16 punch-throughs on both sides of the silicon detector surrounding the active area. The advantages of this structure is that the active area is shielded from the surface, edge leakage currents are controlled as well and a gradual drop of the potential from the detector rim towards the potential of the undepleted substrate is provided. The layout of one corner of the silicon wafers n-side is displayed in figure 3.5, [Abt99].

3.3.2 Frontend Electronics

The silicon micro strip detector and the APV25[1] readout chips are glued onto two L-shaped 6-layer PCBs[2], called "L-board". Onto these L-boards the connections for data transmission, power lines, a configuration bus clock and trigger information as well as pads for the silicon bias voltage are provided. The two boards are on different potentials due to the depletion voltage. The 1280 channels on the *n*-side and 1024 channels on the *p*-side of the detector are bonded to 10 and 8 APV25 read out chips, respectively, with 128 channels each. The APV25 readout

[1] **A**nalogue **p**ipeline, **v**oltage-type
[2] **P**rinted **C**ircuit **B**oard

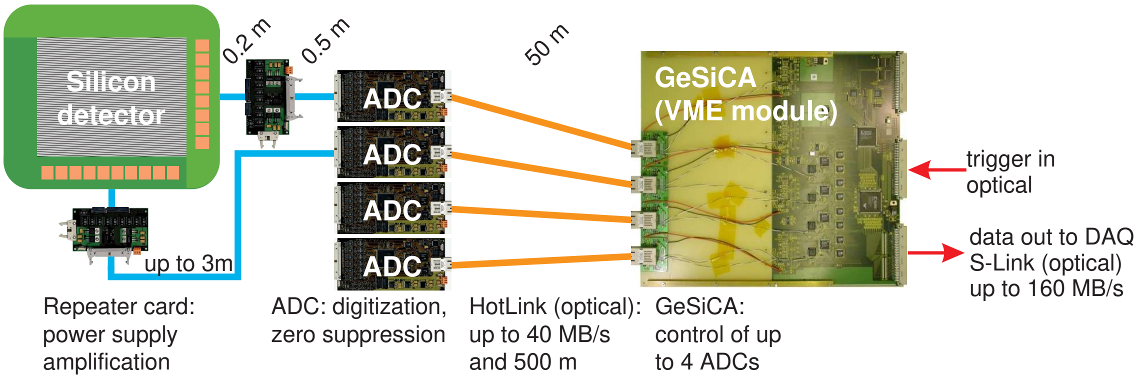

Figure 3.6: The silicon readout chain [Wag01]

chip is an analogue pipeline ASIC intended for read-out of silicon strip detectors in the CMS silicon trackers at LHC[3] at CERN. The chip amplifies signals from the silicon detector and samples them continuously every 25 ns. Each channel of the APV chip consists of a low noise CR-RC type shaping amplifier which reshapes an arriving charge cloud into an well defined voltage pulse with $\sim$ 50 ns rise time. The analog samples are stored in a 160 element deep analog pipeline which gives a maximum trigger latency of 4 μs at 40 MHz sampling rate. If a trigger pulse arrives the analog samples are read out and multiplexed onto a single differential output. The APV chips are connected to the repeater card. This card supplies the chips with power and amplifies the signal. It also provides trigger and clock lines. The amplified signal coming from the APV chip is digitized in the ADC card, by one ADC card for each detector side. This card is reducing the amount of data by suppressing channels with signals under a certain threshold ("zero suppression"). The so called GeSiCA[4] VME module can multiplex the data of up to four ADC cards into one serial data stream, which goes via optical S-Link[5] to the DAQ[6] computer. The setup of the frontend electronics is shown in figure 3.6 and a detailed description can be found in [Gru01, Wag01].

[3]**L**arge **H**adron **C**ollider

[4]**Ge**M and **Si**licon **C**ontrol and **A**cquisition

[5]S-LINK is a CERN specification for an easy-to-use FIFO-like data-link which can be used to connect front-end to read-out at any stage in a data flow environment [Bij01]

[6]**Data****Aq**uisition

Chapter 4

Modifications of the cryogenic Silicon Detectors

During the 2002 and 2003 beamtime the COMPASS experiment has been operated with a high intensity beam of $4 \cdot 10^7$ muons/s with an energy of 160 GeV. In future a hadron beam with a ten-fold higher particle-flux density is foreseen. This leads to a radiation dose of 150 kGy per year, that means the lifetime of a silicon detector will be limited to one beam time. The Lazarus effect predicts an increase of the charge collection efficiency (CCE) of a radiation damaged silicon detector at 130 K. To be prepared for the hadron beam, a silicon station for cryogenic operation was developed. The main principle is to cool the silicon detector with liquid nitrogen running along the silicon wafer in a thin capillary. In this chapter neccessary modifications and developments to go from warm to cryogenic operation of the silicon detector are described as well as the used cryogenic setup.

4.1 Frontend Electronics

The silicon wafer is glued with a special single component silicon glue to the L-board. A nice property of the glue is its elasticity to absorb thermally induced and mechanical stress. The L-board provides connections which are required for cooling. A thin Cu/Ni capillary through which liquid nitrogen flows (diameter $d_{outer} = 1.6$ mm, $d_{inner} = 1.3$ mm) is soldered on the back side of the L-board. The heat flow from the silicon wafer to the capillary is supported by copper layers of the L-boards and additional metalized holes. The readout chips are thermally decoupled from the silicon to constrain significantly the heat flow of the readout chip. That is very useful because the readout chips are a major heat source with

0.4 W each. Accumulated that are 4 W along the n- and 3 W along the p-side of the silicon detector which are dissipating uniformly on this two sides of the L-board[A+03].

The APV25 readout chip is originally not designed for cryogenic operation. At 130K the readout chips need a higher nominal than in warm operation at room temperature. It is experimentally observed that the APV chip needs ± 1.3 V at cryogenic operation instead of ± 1.25 V under standard conditions. Therefore the power supply for the APV chips on the repeater card had to be modified. Some characterisations of the APV chips were done at different temperatures and stability checks of noise, pulse shape and output data format after 50 thermal cycles. An increase of the signal amplitude is observed and the rising time of the signal is 15% faster compared to room temperature. [A+03].

In order to take advantage of the Lazarus effect, the temperature of the silicon has to be well controlled. The temperature distribution of the complete setup was simulated numerically. Due to the high thermal conductivity of silicon it could be shown by simulations that it is sufficient to cool only on two edges of the silicon wafer instead of four [A+03]. The hottest point on the silicon wafer is opposite the cooling capillary. On this corner there is a Pt100 with thermal conductive paste mounted. At CERN the Pt100 are connected to an ELMB[1], there the values are read out via the COMPASS slow control system (DCS).

4.2 Cryostat and Cooling Facilities

For cryogenic operation a vacuum around 10^{-5} mbar is needed mainly for thermal insulation and to prevent icing on the surface of the detector. The cryostat is made of stainless steel and has a size of $240 \times 240 \times 82\,\mathrm{mm}^3$. On both sides there are aluminum flanges with big opening areas ($260\,\mathrm{cm}^2$). These detector windows consist of a support structure of Kevlar wires covered with metalized mylar foil. A detailed discussion of the detector windows is given in chapter 4.3. The cryostat was designed to have enough space for feedthroughs for liquid nitrogen, electrical connections as well as connectors for a vacuum gauge and the pumping station. The electrical connections are realized in so called "flange flies". Two special shaped PCB connectors are sticked with epoxy glue onto aluminum flanges with two thin feedthroughs. The connectors for the liquid nitrogen supply are made in a way that they are vacuum tight. Components made of Delrin decouple the cryostat electrically from the vacuum pump and gauge because the cryostat is connected to the same groundig potential of the silicon.

[1] **E**mbedded **L**ocal **M**onitor **B**oard

The main part of the cooling facilities in the cryostat is the capillary running along the two sides between the silicon wafer and the readout chips. For heat transport optimization the pads on the L-board, where the APV readout chips are glued to, are connected to the localized copper layers in the PCB. These copper layers are connected to the bias voltage of the silicon wafer. One cooling capillary is used for one silicon wafer, that means the two sides have to be electrically insulated. A special connector was designed with a feedthrough fitting the external diameter of the capillaries. The connector is casted in a nonconductive epoxy glue and sticked to the capillaries with the same type of glue [$A^{+}03$]. To be electrical decoupled from the liquid nitrogen distribution there is an additional ceramic insulation tube with the diameter of the capillary soldered in series. A photograph which shows all the cooling facilities and the silicon detector in the cryostat can be found in the appendix B.1.

4.3 Detector Window

The detector window, which is needed for cryogenic operation has to satisfy special demands. On the one hand it has to be vacuum and light tight and on the other hand beam particles should pass the detector windows as unaffected as possible. Thus, the mass density and the leakage rate have to be as low as possible.

4.3.1 Functional Principle

The current design of the detector window is based on the previous layout developed at the TUM, hence it is improved by additional ideas. A detector window which has to fulfill similar properties described above has been devised at the Institute for Nuclear Physics in Mainz [Sau95]. For the spectrometers of the A1 collaboration, windows were designed which consist of mylar[2] foil glued on Kevlar[3] yarn. This basic idea inspired our development of a vacuum tight detector window. The guiding concept is to arrange the Kevlar yarn, see figure 4.1, in a special way as a support structure (Kevlar mesh) to take the force caused by the atmospheric pressure and to use an aluminum metalized mylar foil, which provides the vacuum and light tightness. The arbitrate advantage of this layout compared to the previous layouts of Munich and Mainz is that the Kevlar yarn never leaves the vacuum side.

[2]Mylar is a polyethylene terephthlate monomer $C_5H_2O_2$[PDG00]

[3]KEVLAR is a fiber of poly-para-phenylene terephthalamide, which was introduced as high-strength KEVLAR aramid fiber in 1971 by Du Pont [KEV]

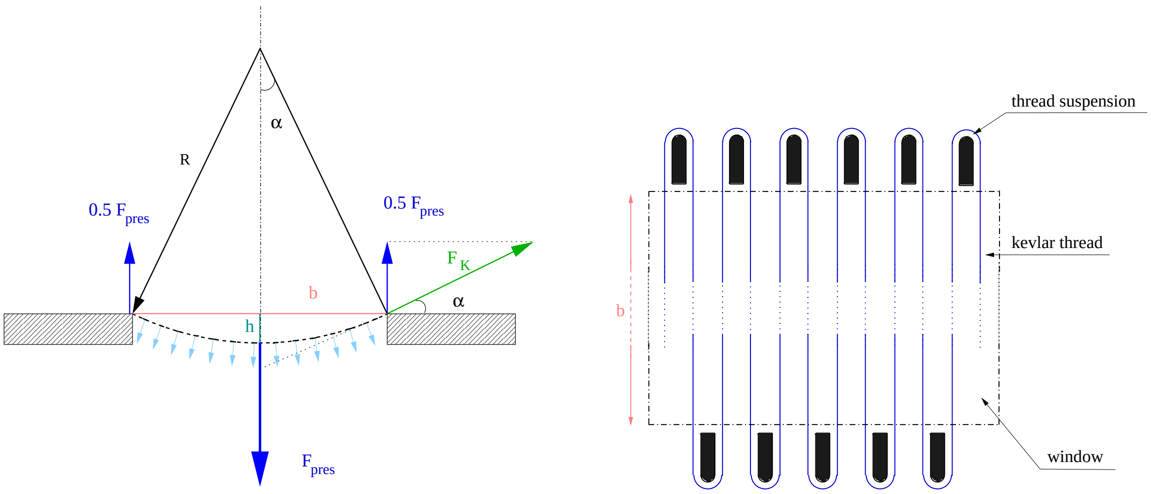

Figure 4.1: **Left:** Force dependencies on the detector window; **Right:** Sketch of the Kevlar support construction

Calculated with an atmospheric pressure p_{at} of 1000 mbar the pressure comes up to 10 N/ cm^2. The force F_{pres}, determined by the atmospheric pressure on the area, held by one Kevlar fiber, yields

$$F_{\text{pres}} = p_{\text{at}} \frac{A}{N}, \tag{4.1}$$

containing N Kevlar wires within the area A of the window. Since the Kevlar yarn and the mylar foil have only a strong resistivity against elonagtion, but are able to deform otherwise, the resulting surface of the window is bended such that the force, exerted by the atmospheric pressure, is always perpendicular to the surface (see figure 4.1). Based on the geometry one obtaines

$$F_{\text{K}} = \frac{1}{2} \frac{F_{\text{pres}}}{\sin \alpha} = p_{\text{at}} \frac{A}{N} \frac{R}{b}, \tag{4.2}$$

F_{K} is the force along the Kevlar yarn, $\alpha = \arcsin(b/2R)$ the angle of the appropriate segment of the circle, R the radius of the bending circle and b the width of the window.

If a maximum bending h for the design is chosen, the radius is fixed, taking into account the elasticity modulus of the Kevlar yarn. Thus force F_{K} can be determined.

bending h [mm]	α	radius R [mm]	5 wires/ cm	2.5wires/ cm	1.25wires/ cm
5	8.2	492.5	98 N	196 N	393 N
10	16.3	250	50 N	100 N	200 N
15	24.2	170.9	34 N	68 N	136 N

Table 4.1: Theoretical values for F_K for different bendings for a detector window of an area of 140×10 mm^2 and for varying Kevlar mesh densities

The smaller the angle α, the higher the force, the Kevlar yarn has to resist and the more mass is needed. For this purpose of the detector window, it is useful to have a very small bending of the window. The space between the cooled detector and the detector window should be as big as possible as these devices are insulated by the vacuum. Otherwise condensed water can appear on the non vacuum side of the detector window. In table 4.1 some theoretical sample values for F_K for different bendings of an area of 140×10 mm^2 and for varying Kevlar mesh densities are calculated. These results have been taken into account for the design of the detector window and later on for several optimizations.

4.3.2 Design

The window is realized by using a 10 mm thick aluminum plate with dimensions fitting the cryostat. The net opening area of the detector window is 260 cm^2 with a maximum length of 200 mm and width of 140 mm. These dimensions are given by the geometry of the silicon detector and the cryostat. Engineering drawings of the detector window can be seen in appendix A. The rounded shape of the window is manufactured in order to reduce the mechanical load on the foil at the edges.

Kevlar support construction (Kevlar mesh) is spanned around the milled riffle structure with 50 riffles on one side and 49 on the other side. In regular distances are drillings to aerate the groove caused by milling the riffles. The Kevlar yarn is fixed on the back with a special fixing construction, see A.2.

Around the window there is an groove for an o-ring. The metalized mylar foil is clamped between the o-ring and a 5 mm thick aluminum flange, which has an opening of the size of the window and is screwed to the detector window plate.

The use of an aluminum metalized mylar foil has several reasons. A thin aluminum layer[4] is necessary to get the mylar foil vacuum tight. An additional 25 μg/ cm^2 aluminum layer is needed to get the detector window light tight as

[4]In our case, we got the metalized mylar foil from TUM Physics Department E12 . This foil has got a 14 nm thick aluminum layer which is sufficient for vacuum tightness.

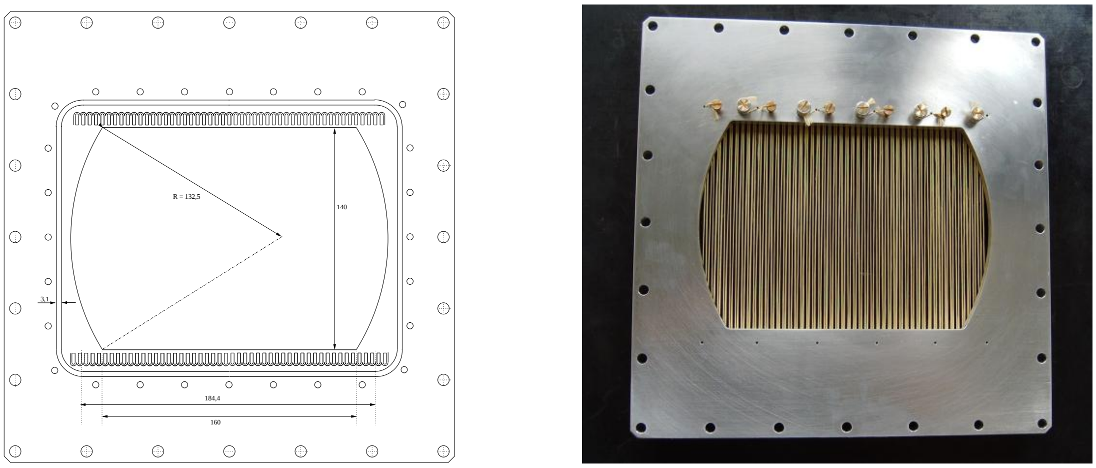

Figure 4.2: Detector window; **Left:** Draft of the front where the riffle structure can be seen, **Right:** photograph of the back, the fixing of the Kevlar yarn can be seen

well as for electrical shielding to get an electrical connection to the cryostat to reduce a possible noise source. The light tightness can easily be proved with the silicon detector. Does the leakage current of the biased silicon detector decrease when the window is covered with an additional light tight foil, then the window has a light leak. But for a mylar foil metalized with 25 μg/ cm^2 aluminum no changes were observed.

First detector window prototypes showed a good performance. The most important aim, getting a high vacuum in the order of $5 \cdot 10^{-5}$ mbar is fulfilled.

4.3.3 Test of single Components

Kevlar Yarn Kevlar yarn is chosen as a material for the support construction because of its very high breaking strength. The available Kevlar yarn has been splitted into smaller yarns with masses of 0.26 g/ m and 0.16 g/ m. For these parts the breaking strength and the elasticity modulus is measured to validate their usability. The experimental setup is shown in figure 4.3, A long piece of Kevlar yarn is fixed on a frame. On the lower end of the Kevlar yarn there is a little noose, to mount a levelling rule perpendicular to the Kevlar yarn. A mass of 11.5 kg is attached on the levelling rule. If the mass is moved along the levelling rule, different forces on the Kevlar yarn arise. On the Kevlar yarn, there are two marks at the top and bottom. For different forces the elongation of the Kevlar yarn can be measured by a second levelling rule, mounted parallel to the Kevlar yarn. Taking the measured values, the elongation can be calculated with Hook's law. The measurement curve for 0.26 g/ m and 0.16 g/ m Kevlar yarn is shown in figure 4.4. The elongation of the Kevlar yarn is plotted in percent against the

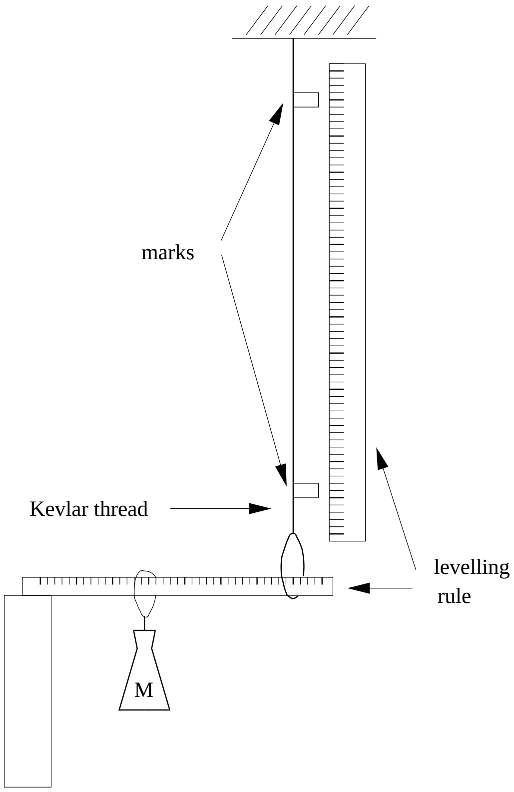

Figure 4.3: Setup for the measurement of the Kevlar elasticity

weight respectively the force on the yarn. For the 0.16 g/ m Kevlar yarn the elongation is about 0.05%/ kg and for the 0.26 g/ m it is 0.07%/ kg. That means a Kevlar yarn of 140 mm and (0.26 g/ m) will be elongated by 0.35 mm by a mass of 5 kg. The elongation of the Kevlar yarn is so little that it is negligible for the manufacturing of the window.

Metalized Mylar Foil Mylar is a polyester film with superior strength, heat resistance, excellent insulating properties and a mass density of 1.39 g/ cm^3. Mylar foil metalized with a thin (14 nm) aluminum layer is vacuum tight and impervious to water. Due to the carbon compound, the radiation length[5] of mylar is very large ($X_0 = 28.7$ cm). These nice attributes of metalized mylar are the reason for choosing this material. To learn more about the properties of metalized mylar, e.g. how much pressure it can stand until it rips, the following setup has been used, see figure 4.5. The foil covers the window without the Kevlar mesh and the o-ring of the detector window plate, and is clamped between a massive aluminum plate of 10 mm thickness and the o-ring. The detector window and the aluminum plate are fixed together by screws. In the middle, a special support,

[5]Radiation length X_0 is the mean distance over which a high-energy electron looses all but $1/e$ of its energy due to radiation . [PDG00]

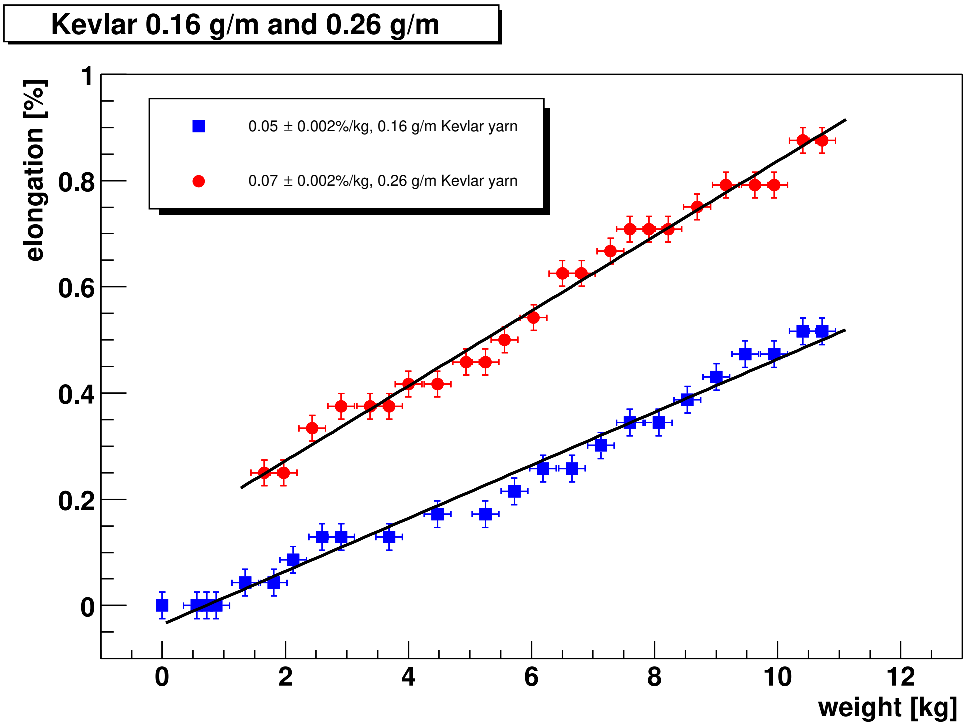

Figure 4.4: Elasticity measurement of Kevlar yarn with 0.26 g/ m and 0.16 g/ m

milled into the aluminum workpiece for a little valve used in inner-tubes is situated. The volume between foil and aluminum valve plate can be flushed by nitrogen gas. A manometer is connected between the valve and the gas bottle. By the pressure reducer on the nitrogen gas bottle, the pressure can be increased very slowly and the foil starts to blow up. The pressure loss on the valve is negligible. At a pressure of 0.8 bar the aluminum metalized mylar foil of 25 μm thickness bursts. The same happens to the 12 μm mylar foil at 0.3 bar. That means, that for the detector window design Kevlar yarn, is defenitly needed as a support.

4.3.4 Test of the Detector Window

To find out the optimized detector window configuration, pressure and leak tests were done.

Pressure Tests The setup used for the pressure test of the complete detector window is the same as the one described in section 4.3.3. But for this test the detector window with Kevlar mesh support was used. Different Kevlar meshes in combination with mylar foils of various thickness were tested. Due to the

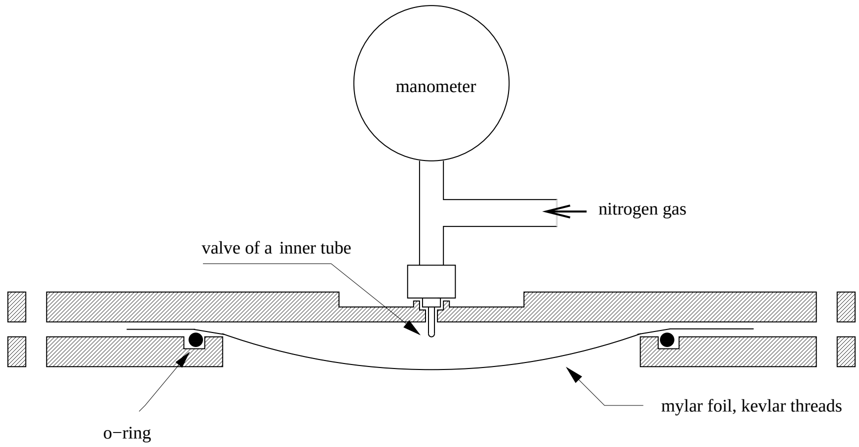

Figure 4.5: Setup for the overpressure test

fact that the detector window configuration 4 (see table 4.3) burst at a pressure of 2.5 bar, further studies were concentrated to lower masses. First, tests with lower Kevlar mesh densities failed, as the Kevlar yarn mainly broke on the lead-throughs drillings because their edges were to sharp and thus cut the yarn. For new tests, the Kevlar mesh was only fixed on one point to reduce the amount of weak points at the lead-through. Burst values for different window configurations are given in tables 4.2 and 4.3.

The tests show that in terms of stability the density of the Kevlar mesh can be reduced to 1.25 yarn/ cm. With the detector window configuration 6.2 (see table 4.3) a long term overpressure test was started. The detector window had to resist against 1.6 bar and burst after three hours. The same test was done with a 25 µm foil (configuration 5). After three hours at a pressure of 1.6 bar, the window was still in a good shape.

configuration	**1**	**2**	**3**		
Kevlar yarn [g/ m]	0.16	0.16	0. 16		
mesh density [yarn/ cm]	1.25	2.5	5		
foil [µm]	25	25	25		
foil mass [mg/cm^2]	3.48	3.48	3.48		
mass yarn [mg/cm^2]	2	4	8		
mass window [mg/cm^2]	5.48	7.48	11.48		
measured values				**blind flange old**	**blind flange new**
leak rate [mbar · l/ s]	—	$8.6 \cdot 10^{-5}$	—	$1.2 \cdot 10^{-4}$	$3.1 \cdot 10^{-5}$
$p_{\mathrm{end,calc}}$[mbar]	—	$4.3 \cdot 10^{-5}$	—	$6 \cdot 10^{-5}$	$1.6 \cdot 10^{-5}$
pressure after pumping [mbar]	60 h $8.3 \cdot 10^{-5}$	23 h $2.9 \cdot 10^{-5}$	36 h $4.5 \cdot 10^{-5}$	20.5 h $5.3 \cdot 10^{-5}$	8 h $4.5 \cdot 10^{-5}$
burst pressure [bar]	1.2	1.8	—	—	—

Table 4.2: Leak rates, calculated end pressure with a 2 l/ s pumpage, measured pressure, calculated end pressure, burst pressure and mass densities of different detector window configurations and blind flanges

configuration	**4**	**5**	**6.1**	**6.2**
Kevlar yarn [g/ m]	0.26	0.26	0.26	0. 26
mesh density [yarn/ cm]	2.5	1.25	1.25	1.25
foil [µm]	25	25	12	12
foil mass [mg/cm^2]	3.48	3.48	1.67	1.67
mass yarn [mg/cm^2]	3.25	3.25	3.25	3.25
mass window [mg/cm^2]	9.98	6.73	4.92	4.92
measured values				
leak rate [mbar · l/ s]	—	$6.4 \cdot 10^{-5}$	$5 \cdot 10^{-5}$	$6.4 \cdot 10^{-4}$
$p_{\mathrm{end,calc}}$[mbar]	—	$3.2 \cdot 10^{-5}$	$2.3 \cdot 10^{-5}$	$3.2 \cdot 10^{-6}$
pressure after pumping [mbar]	72 h $1.5 \cdot 10^{-5}$	26 h $6.2 \cdot 10^{-5}$	24 h $3.6 \cdot 10^{-4}$	20 h $4.0 \cdot 10^{-4}$
burst pressure [bar]	2.5	1.6	1.6	1.8

Table 4.3: Leak rates, calculated end pressure with a 2 l/ s pumpage, measured pressure, calculated end pressure, burst pressure and mass densities of different detector window configurations.

Leak Test To measure the leak rate of the detector window flanged on the cryostat, the “rise-in-pressure-method” is used. In figure 4.6 the test setup is schematically shown. The test item is evacuated and between the vacuum pump system and the test item, a valve is installed, which is closed before starting the leak rate measurement. The pressure is read from the vacuum gauge at different time intervals. At the beginning, the pressure rises very fast, due to desorption (like evaporation of impurities in the cryostat). After a certain time, it falls in a steady-state.

The leak rate is the amount of gas, inflowing per time unit. At a constant temperature, the inflow of gas is given by the law of Boyle-Mariotte which is the product of the volume V and the pressure p, except a proportional factor. The measured leak rate L is the pressure change Δp at a constant volume V (volume in the cryostat) and at temperature per time Δt:

$$L = V\frac{\Delta p}{\Delta t} \tag{4.3}$$

This comes up to a volume change per time unit at a constant pressure

$$\frac{\Delta V}{\Delta t} = \frac{L}{p_{\mathrm{const}}}. \tag{4.4}$$

This volume change results from the the pump and $\Delta V/\Delta t$ is called the effective pumpage S_{eff}. p_{const} is the end pressure, p_{end}, of the setup, when an equilibrium between the gas inflow through leaks and desorption and the pump capacity is existing.

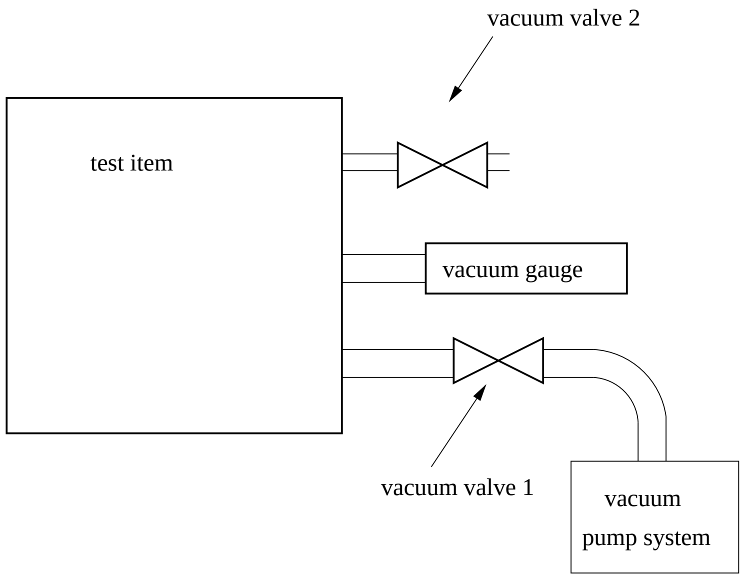

Figure 4.6: Setup for the vacuum leak test rate measurement

The total pumpage of the used pumping station is $S = 33\,\mathrm{l/\,s}$. But to get the effective pumpage S_{eff} of the pumping station the conductances C of the used corrugated tube ($C_{\mathrm{tube}} \propto d^3_{\mathrm{diam}}/l_{\mathrm{tube}}$), reducing spout and valve have to be taken into account. All this components can be estimated roughly by a 85 cm long tube

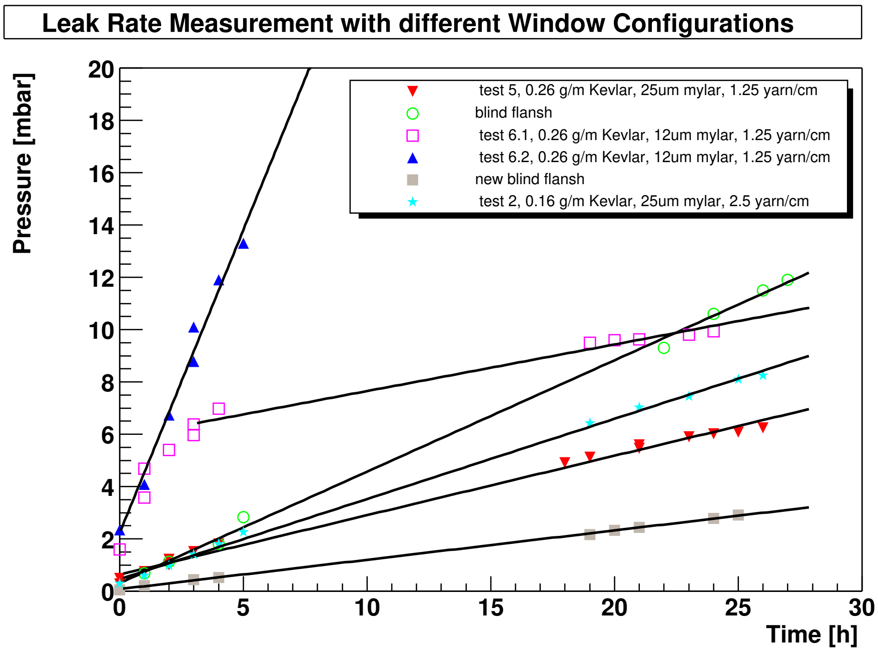

Figure 4.7: Leak rate measurement of two different blind flanges and detector window configurations

and a reduction of a diameter of 40 mm from the turbo pump outlet to 25 mm diameter of the connected reducing spout. The effective pumpage can be calculated by

$$\frac{1}{S_{\text{eff}}} = \frac{1}{S} + \frac{1}{C_{\text{tube}}} + \frac{1}{C_{\text{red}}} = \frac{1}{33\,\text{l/ s}} + \frac{1}{2.2\,\text{l/ s}} + \frac{1}{54.9\,\text{l/ s}} \to S_{\text{eff}} = 2.0\,\text{l/ s}. \quad (4.5)$$

With the leak rate L the end pressure can be determined by $p_{\text{end}} = \frac{L}{S_{\text{eff}}}$.
All the measured leak rates, calculated end pressures and measured vacuum pressure values of the tests are summarized in tables 4.1 and 4.2. In figure 4.7 the measured change of pressure is plotted versus the time, for different window configurations and blind flanges. It can be seen that for the window in test configuration 6.1, the leak rate is one order of magnitude higher than for configuration 6.2. Further there is an exponential rise in the beginning of the measurement is due to desorption. In general window configurations with 12 µm foil showed the worst leak rates. Most likely the foil is to thin there to be clamped tight enough. The leak tests for two different blind flanges point out, how important polished sealing surfaces are. The old blind flange had already scratches. All the other window configurations showed a stable behavior. There leak rates and measured pressure are in the same order. The difference in the values may also arise from different well polished sealing surfaces.

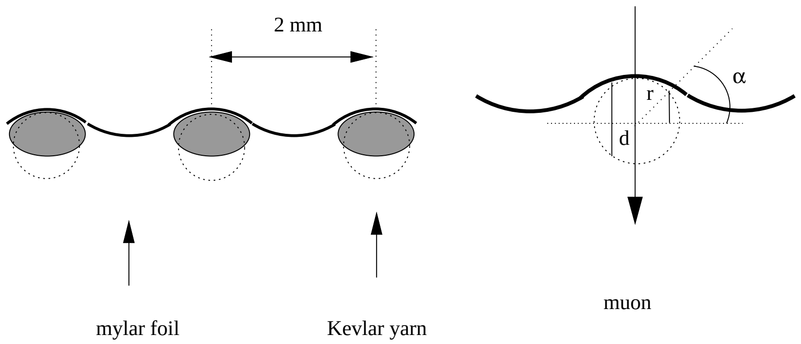

Figure 4.8: Profile cut of the Kevlar mesh; the pressure presses the foil onto the Kevlar mesh and deforms it, but for the calculation of d the Kevlar yarn is assumed to have a circular cross section

4.3.5 Radiation Length

A very important parameter of the detector window is its radiation length. For this value, the geometry of the Kevlar mesh has to be taken into account, see figure 4.8. The radiation length depends strongly on the place, where the beam particle passes the detector window.

One single Kevlar yarn has a length density ρ_l of 0.16 g/ m or respectively, 0.26 g/ m and a volume density ρ_V of 1.45 g/ cm^3. The cross section A_a of the Kevlar yarn is

$$A_a = \frac{\rho_l}{\rho_V}. \tag{4.6}$$

If the shape of the Kevlar yarn is assumed to be circular then the Kevlar yarn radius is given by $r = \sqrt{A_a/\pi}$. For a traversing particle the effective length through the Kevlar yarn depends on its distance from the center of the yarn:

$$d = 2r_{max} \sin\alpha = 2\sqrt{A_a/\pi} \cdot \sin\alpha. \tag{4.7}$$

In table 4.4 the radiation lengths of the two different mylar foils and Kevlar yarns are given, along within the maximum diameter of Kevlar yarn used for this case. For the Kevlar yarn, the radiation length of Kapton was used, as they have very similar mass formulas. Due to the fact that the radiation length is on the maximum diameter about half of that of the silicon wafer it is necessary to reduce the Kevlar mesh density. Effects of multiple scattering are discussed in more detail in 5.3.5.

Mylar	**R.L.** X_0
25 μm	$8.7 \cdot 10^{-5} X_0$
12 μm	$4.2 \cdot 10^{-5} X_0$
Kevlar	
ρ_l 0.26 g/ m	$1.76 \cdot 10^{-3} X_0$
ρ_l 0.16 g/ m	$1.36 \cdot 10^{-3} X_0$
Silicon	
300 μm	$3.2 \cdot 10^{-3} X_0$
600 μm	$6.4 \cdot 10^{-3} X_0$

Table 4.4: Material budget in units of radiation length X_0

4.3.6 Discussion and Outlook

In recapitulation, the development of the detector window was very successful. It is fully functional and fulfills all specifications. The reachable vacuum, owing values of approximatery $5 \cdot 10^{-5}$ mbar for different detector window configurations, is in the same order, the cryostat reaches by using blind flanges. Due to the aluminum layer on the mylar, the detector window is light tight and no significant noise induced by the window on the detector could be observed.

By the overpressure tests one weak point of the construction could be observed. The edges at the lead-through drillings for aeration are too sharp. Thus at overpressure the Kevlar yarn is cut by these edges and therefore the window bursts. One of the first prototype of these detector windows was used for three month in the test setup of the laboratory. This window had around forty pump cycles before it was disassembled. Especially on these sharp edges described above, the Kevlar yarn showed signs of wear.

Due to the fact that the Kevlar mesh never leaves the vacuum side and that the mylar foil is clamped between an o-ring and a flange, the handling is very uncomplicated. It is very easy to exchange the different components compared to detector windows, where the foil and the support is glued onto the flange.

During the COMPASS 2003 muon run, two detector windows built up by the 0.16 g/ m Kevlar yarn and 25 μm metalized mylar foil were installed at the silicon station meant for cryogenic mode of operation. The detector window was in use in warm as well as in cryogenic operation. In general the big opening area (260 cm^2) of the detector window is a big advantage also for the silicon stations in warm operation. In warm operation, the silicon station is flashed with nitrogen gas (max. pressure approx. 0.7 bar) to cool the APV chips. These detector windows can be mounted vice versa and take advantage of the Kevlar mesh support.

By this the detector window design, it was also possible to keep the mass density low at 11.5 µg/ cm^2 for the windows which were used in this beam time. By the overpressure and leak rate measurement could be shown that it is possible to reduce the mesh density. The lowest mass configuration with good properties has a detector window with 0.26 g/ m Kevlar yarn and 1.25yarn/ cm Kevlar mesh density.

4.4 Laboratory Setup for cryogenic Operation

A self-pressurizing dewar with a volume of 120*l* volumetric capacity of liquid nitrogen and 1 barworking pressure provides the liquid nitrogen supply. A low loss transfer-line connects the liquid nitrogen inlet of the cryostat to the dewar. This transfer-line itself is cooled by liquid nitrogen. The transfer-line is made in a way that part of the liquid nitrogen flux flows the transfer-line back. The transfer-line consists of three different tubes. The outer one is a evacuated flexible tube for insulation. The inner one is the liquid nitrogen supply for the silicon. In the second tube, which covers the inner one, is the flow back of a part of the liquid nitrogen for cooling the inner tube. The flux of the nitrogen flow back is regulated with a manual flowmeter. The vacuum tight connector for the transfer-line is the nitrogen inlet. It is connected to the capillary which furcates in the cryostat. The nitrogen gas leaves the station through the capillaries and a special outlet connector. The nitrogen flux is regulated by two remote controlled Bronkhorst mass flowmeters, one for each detector, two per silicon station. The flux which is needed to cool down the detector is measured to $200 - 500$ l/ h nitrogen gas.

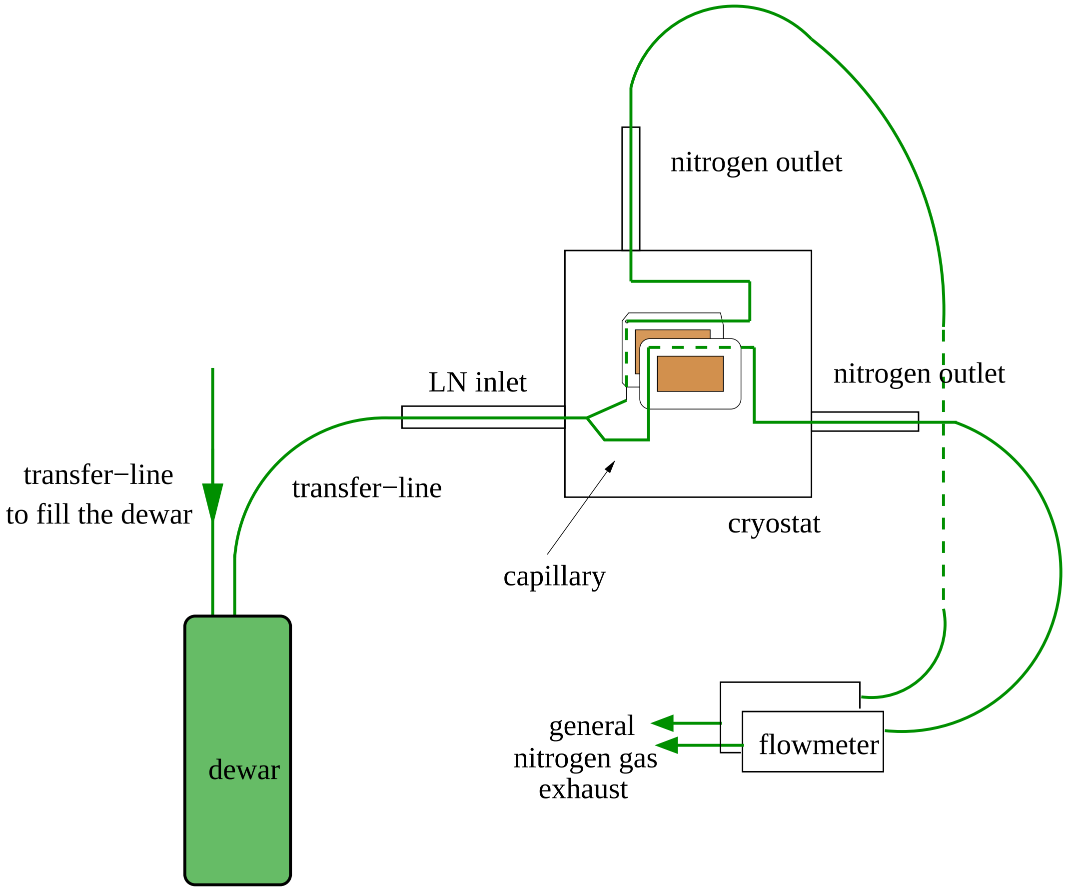

Figure 4.9: Cryogenic setup of the laboratory, which was used during the 25ns beam

Chapter 5

Silicon Detectors in COMPASS Beamtime 2003

This chapter starts with an overview on the setup and leakage current trending during the COMPASS muon run. In the second part the commissioning of one silicon station in cryogenic operation during the COMPASS 25ns run is described, which is a low intensity muon beam where the time structure of the beam is pulsed. The hardware setup is discussed, the temperature trending and and problems which appeared. In the analysis part tracking and alignment procedure, the spatial resolution of the silicon detectors and first results of the comparison between warm and cryogenic operated silicon detectors are presented.

5.1 Silicon Detectors during Muon Run

5.1.1 Setup

For the COMPASS muon run 2003 three silicon stations, as described in chapter 3.3, were installed. These silicon stations are located upstream of the polarized target region. They are sandwiched between two stations of scintillating fibers. These tracking detectors, the silicon microstrip detectors and scintillating fibers are needed for beam definition. A draft of the setup is given in figure 5.1. A picture of the setup at CERN is shown in appendix B.2.

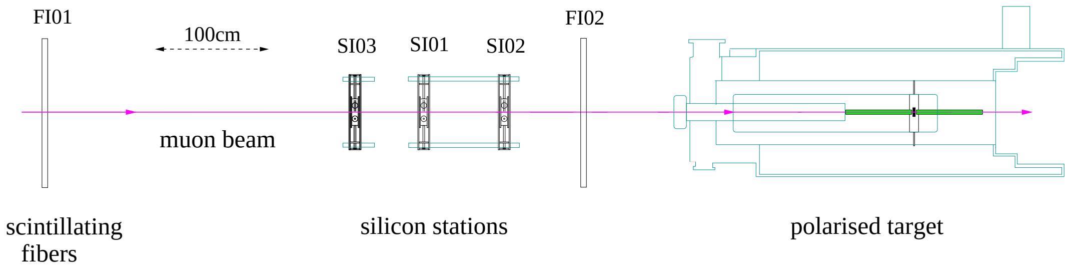

Figure 5.1: Silicon detectors in COMPASS

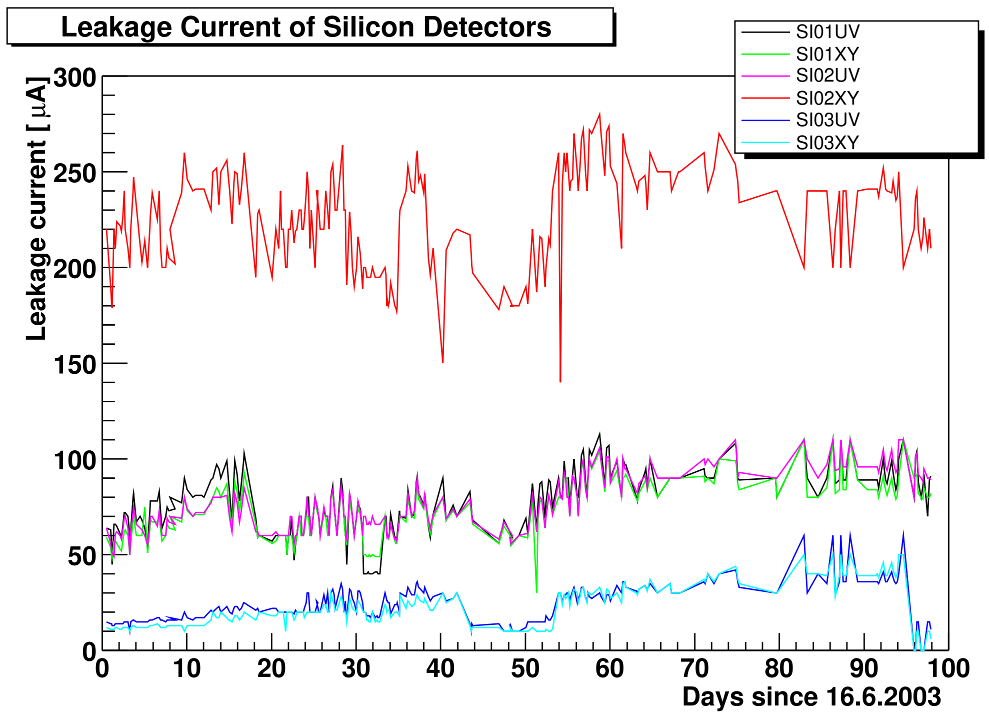

Figure 5.2: Leakage current trending of the silicon detectors during the COMPASS beamtime 2003

5.1.2 Leakage Current Trending

During the beam time 2003, ISEG high voltage modules were used for biasing the silicon detectors. Before, the biasing was done by batteries. The new ISEG modules provide additional online monitoring of the silicon detectors leakage current, so for the first time it was possible to survey the leakage current of the silicon detectors. Unfortunately it was not possible for this beam time to integrate the ISEG modules into the COMPASS slow control and its data base. The leakage current values were only monitored on an external computer and values were written down three and to six times per day by the COMPASS shift crew. Nevertheless some major tendencies can be seen in figure 5.2. The big temperature dependency of the leakage current as it is mentioned in chapter 3.1.4 can be seen in the oscillations between day and night. The amplitude of the oscillations is in the order of $10 - 15\%$ of the current average value. Also a slow increase of the leakage current over the whole beam time can be observed.

The silicon detectors of station SI03 have been used for the first time. These detectors were already fully depleted at a bias voltage of 60 V on the SI03UV and 50 V on the SI03XY detectors. In the beginning of the beamtime the leakage current was for both detectors in the order of 14 μA, and at the end 45 μA were reached. This is a clear sign of radiation damage at a fully depleted silicon detector. The sudden drop of the leakage current at the end of the beam time is due to the cryogenic operation of SI03 at 130 K.

The first and second silicon station (except SI02XY detector) were biased with 110 V. They have been in use for the third beam time. They already suffer from radiation damage. Their initial leakage current was in the order of $50 - 60$ μA and rose up to 100 μA over the beamtime. The detector SI02XY shows a leakage current of about 220 μA and was operated at 100 V. In the SINTEF silicon wafer specifications, the higher leakage current is mentioned. That means the high leakage current is not only a phenomenon of radiation damage. The break of the muon beam during the days $44 - 52$ of the beam time by a decrease of the current is seen in figure 5.2. Due to less power consumption of the APV chips without beam, the temperature on the silicon is lower.

5.2 Silicon Detectors in cryogenic Operation

5.2.1 Hardware Setup

The silicon station SI03 was installed at CERN in the middle of June 2003. The detectors were operated warm all the beamtime except for a short period from end of July until beginning August where first cryogenic tests were accomplished. For the liquid nitrogen supply a fixed installation was planned. The liquid nitrogen supply was planned to consist of a transfer-line running from the COMPASS liquid nitrogen distribution box on the gallery of the experimental area to a valve box, which distributes and regulates the nitrogen flux. For the vessel of the valve box the CERN TIS approval was denied and the vessel has to be redesigned. Since this was not possible for this beam time, it was decided to install the laboratory setup at CERN as described in chapter 4.4.

The CERN cryogenic group installed a nitrogen transfer-line from the COMPASS distribution box to the self pressurizing dewar brought from Munich. With this installation, the dewar could be refilled. A camera monitored the level meter, the pressure manometer for the dewar as well as the flowmeter regulating the flux for cooling the transfer-line. The temperature of the silicon could be seen by the COMPASS slow control, but there was no control of the pressure in the cryostat. The flowmeters were remote controlled from outside of the experimental area. The maximum operation pressure on the self pressurizing dewar was limited by a safety valve to 1.5 bar. The nitrogen consumption was 1000 l/ h nitrogen gas in total. To keep the silicon detectors at 130 K, the estimated value of 500 l/ h nitrogen gas has been used, but the same amount was needed to cool down the transfer-line running between the dewar and the cryostat. A pumping station having a pumpage of 33 l/ s was connected by a 110 cm corrugated tube to the cryostat and to a vacuum gauge. This long corrugated tube with the diameter of 2.5 cm reduced the effective pumpage down to 1.5 l/ s, see equation 4.5. Due to the mechanical constraints, a better solution was not available this year. The cryogenic setup can be seen in figure B.3.

5.2.2 Temperature Trending

In the period 18. - 22. September the SI03 was operated in the cryogenic mode below 145 K for approximately 32 hours in total. During periods of five to eight hours with stable conditions, data with electron and muon beam were taken with different bias voltages and latencies on silicon station SI03.

In the temperature curve depicted in figure 5.3 of silicon station SI03 starts at 55° C. This is a typical value for standard operation during the last hours of the COMPASS physics muon beam. On 17. of September the machine development started and silicon station SI03 was shut down for preparing cryogenic operation. There can be seen the ambient temperature with a short interruption of a cooling test. Some time was needed to get the cryogenic system stable running for longer time. In the evening of the 19. first data could be taken under very stable condi-

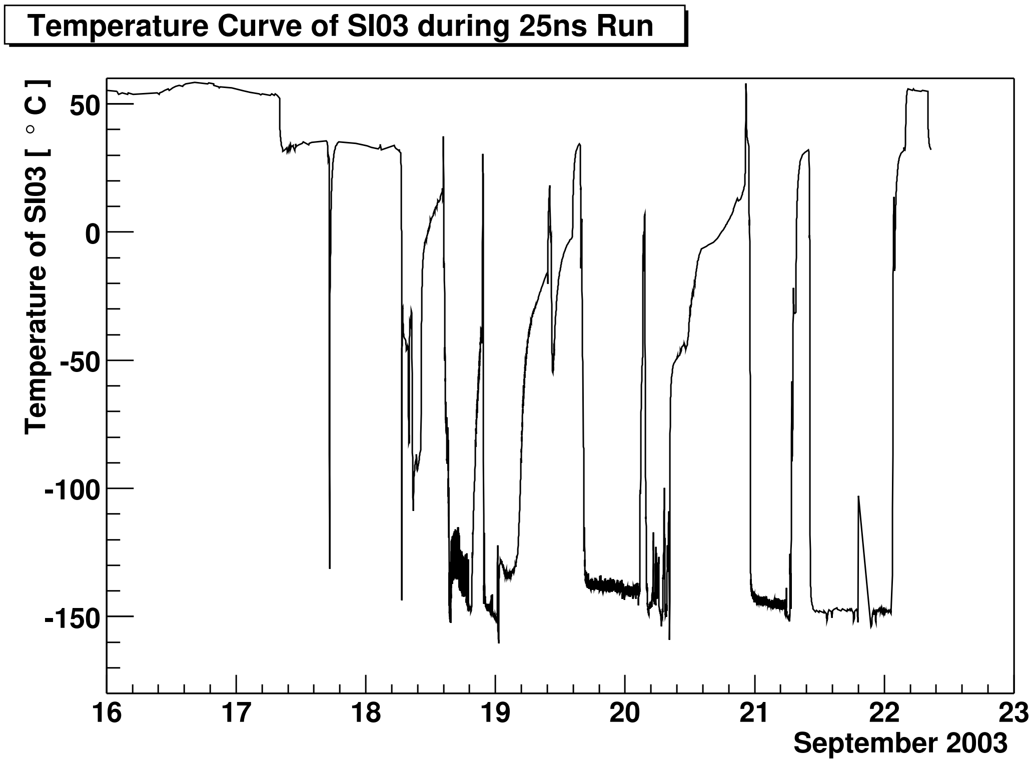

Figure 5.3: Temperature trending during the 25 ns beam of the silicon station SI03

tions. Between the 20.- 21. there has been a break due to refilling the dewar. One phenomenon that appeared very often was that the transfer-line between the dewar and the cryostat started to warm up. A possible explanation is water (crystal) impurity in the nitrogen blocking the tube after some time. This is investigated at the moment. It was only possible to solve this problem this problem by a manual intervention inside the experimental area. The warming up and waiting times for getting access can be observed very well by the temperature curve.

5.2.3 Problems during 25 ns Run

On the way to commission the silicon station in cryogenic operation some weak points have been found. In August, a vacuum of $8 \cdot 10^{-5}$ mbar in cryogenic operation was reached by this setup. A better result was not possible, because of the low pumpage. During the 25 ns beam a pressure of only $8 \cdot 10^{-3}$ mbar was reached during cryogenic operation. Vacuum leaks were observed on the capillaries and at the feedthroughs of the nitrogen gas outlets. Due to too large mechanical stress on the capillaries they broke and had to be soldered. Additionally the o-rings on the nitrogen gas outlet got brittle due to several thermal cycles but they could not be exchanged due to mechanical constraints. That means that during the 25 ns run it was not possible to improve the vacuum. The necessary reengineering of the nitrogen outlets is ongoing in the time where this thesis is being finished.

Due to the laboratory setup a continuous cryogenic operation was not possible. The transfer-line warmed up after at least six to ten hours of cryogenic operation, because of pressure loss in the dewar. This problem could be solved by increasing the flux of the nitrogen flow back of the transfer line or by refilling the dewar, even though it was not empty. Further a leak at the level meter of the dewar was observed which could not be repaired.

5.3 Data Analysis

5.3.1 Alignment and Tracking

In order to analyze the spatial and time resolutions, the efficiencies and the signal shape of the silicon microstrip detectors it is very important to have a precise alignment in order to get a good track reconstruction upstream of the polarized target. In this region the circumstances are definite. There is no electromagnetic field and the beam particles are crossing the tracking detectors in a straight line, except deflections due to multiple scattering, e.g. in the silicon detectors. Each detector should monitor the hits, caused by the incident beam particles. In the silicon detectors mainly two different cases can be observed, that the collected charge Gaussian distribution is spread over one or two strips, respectively. The hits from close-by strips are combined to one cluster signal. The position of the cluster signal is derived from the amplitude-weighted mean of the position of the hit strip. For a single strip event the position of the cluster is the center of the strips.

For each event[1], which is read out there, the cluster of the passed beam particle and several clusters due to detector noise can be found. The number of observed clusters per event is called cluster multiplicity. Together with the information about the clusters and their positions, the track of the beam particle can be reconstructed. The arrangement of tracking detectors in front of the target is shown in figure 5.1.

In order to determine the tracks of a beam particle with the measured clusters in reference to the COMPASS coordinate system, the positions and orientations of

[1]If muon passes the COMPASS spectrometer there is a special system of hodoscopes to build a trigger. This trigger is the signal for the frontend electronic to read out all the detectors. This defines an “event”.

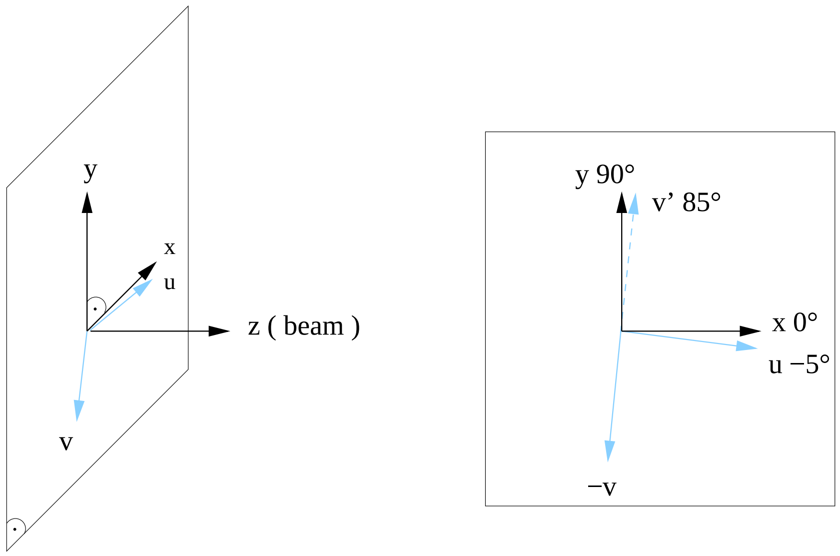

Figure 5.4: Coordinate system of COMPASS

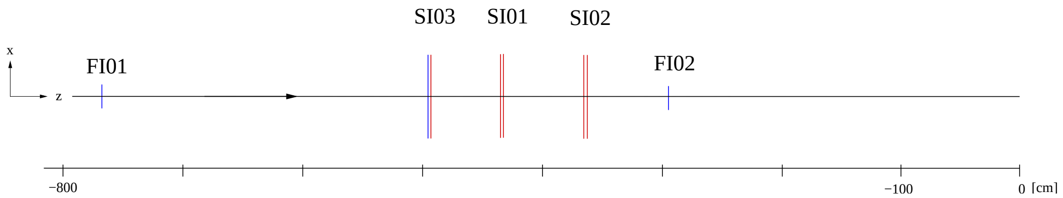

Figure 5.5: Tracking setup for beam definition

all tracking detectors involved have to be known, with respect the appropriate coordinate system. In each silicon station, one detector has a X and Y projection. To reduce ambiguities caused by multi-hit events the second silicon detector in each station has a U and V projection which are inclined by an angle of 5° in respect to X and Y, see figure 5.4. The V projection is defined to have a negative sign.

Tracking In general the tracking is done by fitting a straight line to the determined cluster positions in three dimensions by taking the least squares method (chi-square minimization). These straight lines (the tracks) are calculated for k clusters per event in n projections, that are k^n possible combinations. There are n measurements x_i for the detectors at the position z_i. Each detector measurement x_i has an error $\sigma_i(i = 1, 2, ..., n)$ which is its spatial resolution. The explicit calculation is given in [W+95].

Alignment The alignment information of the detector positions are stored in the COMPASS detectors geometry files for certain periods of the beamtime. Due to the fact that the whole official COMPASS alignment is still in progress for parts of the beamtime it was necessary to do the alignment of the silicon and scintillating fiber stations upstream of the polarized target. For this task it is convenient to use the COMPASS online analysis program COOOL written by Colin Bernet and Damien Neyret (CEA, Saclay).

During the alignment, the tracking was done by using the two scintillating fiber stations, FI01 and FI02, as well as the silicon detector SI01UV of silicon station SI01, see figure 5.5 to reduce ambiguities. In the middle of the first and the last detector which takes active part in the tracking, the beam profile is reconstructed. The very first step was to center the beam in moving all the three tracking detectors in the geometry file about the same value in x and y the beam misses the center.

The beam divergence is equal to the angle of the beam, with respect to the z-axis. In general the beam is expected to be parallel to the z-axis. Thus the beam divergence is distributed about the center. The second step in alignment was to correct the rotation angle of the detectors.

Whether the alignment is well done can be seen when the χ^2/ndf of the fitted track is close to 1 and by checking the χ^2 probability distribution. If the correct Gaussian error is assumed and the influence of multiple scattering is small, this distribution has to be flat. To improve the alignment, one silicon projection, e.g U-projection, was fixed and the other one, V- projection was moved about a certain value. There was done for several iterations to get the position with the minimum value of χ^2. At this value this projection was fixed and the other projection of the silicon detector was moved to determine its best position. Then also the residuals of the detectors which are active in the tracking are distributed about zero. It is convenient to do this calibration on the silicon detector placed between the scintillating fiber stations, as due to the centered beam divergence, it is known that the scintillating fiber stations are placed correctly to each other. Since the silicon detectors have a resolution with is about a factor of 10 better spatial resolution compared to the scintillating fibers, the silicon detectors have the biggest weight in the χ^2 calculation.

Having a good tracking, one can have a look at the residuals of the detectors, which did not take part in the tracking. The position of the residuals of these detectors is the value one has to move these detectors into the track position, because usually they are displaced about a certain distance. The accuracy in calibrating these detectors into the track was better than 3 μm.

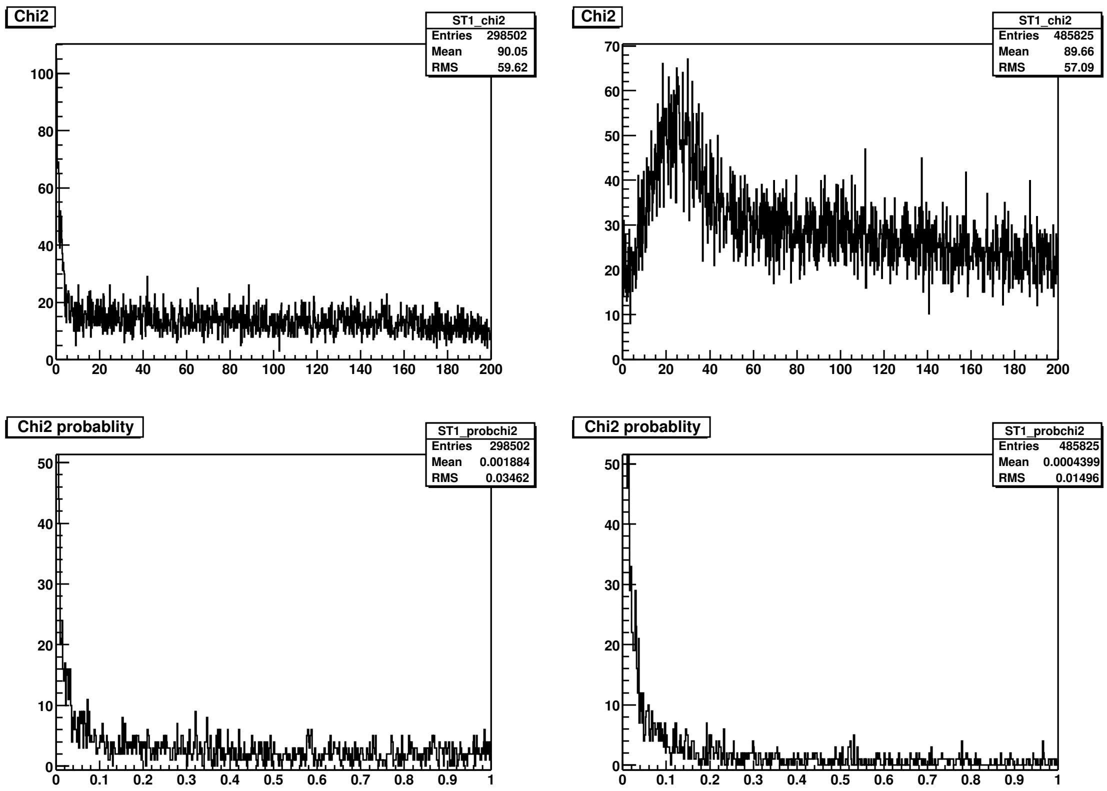

Figure 5.6: The χ^2 distribution and the χ^2 probability distribution both after the alignment on the left and during the alignment on the right

In figure 5.6, the χ^2 distribution and the χ^2 probability distribution of run 31615 are displayed both after the alignment on the left side and during the alignment on the right side. After the alignment the χ^2 distribution shows the characteristic shape. This good χ^2 probability distribution well aligned shows a flat distribution up to a very narrow peak to small values at zero. In the non-aligned plot the distribution is shifted to little values. That means, the errors on the detectors are estimated to good for that bad alignment.

5.3.2 Beam Reconstruction with Silicon Trackers

In the analysis program COOOL a cut in this χ^2 can be set to collect only the good tracks with low χ^2. The alignment procedure was precisely done for the run 31615. With good alignment and tracking the beam profile of the COMPASS muon beam can be reconstructed with three silicon detectors only. From each silicon station one silicon detector is used for tracking (two UV-projections and one XY-projection and vice versa). The reconstructed beam profile for silicon station SI02 X/Y plane is shown in figure 5.7. The σ of the beam is

$7.7 \pm 0.1 \times 9 \pm 0.1$ mm^2 RMS which is in the order like it is mentioned in chapter 2. The beam is not centered in this projection, because the silicon station was installed with a 5 mm shift in x-axis. The beam divergence profile shows an angle of (0.049 ± -0.004 mrad) in x and (-0.093 ± 0.007 mrad) in y direction. The width of the beam divergence distribution is (0.420 ± 0.003 mrad) in x and (0.680 ± 0.005 mrad) in y direction.

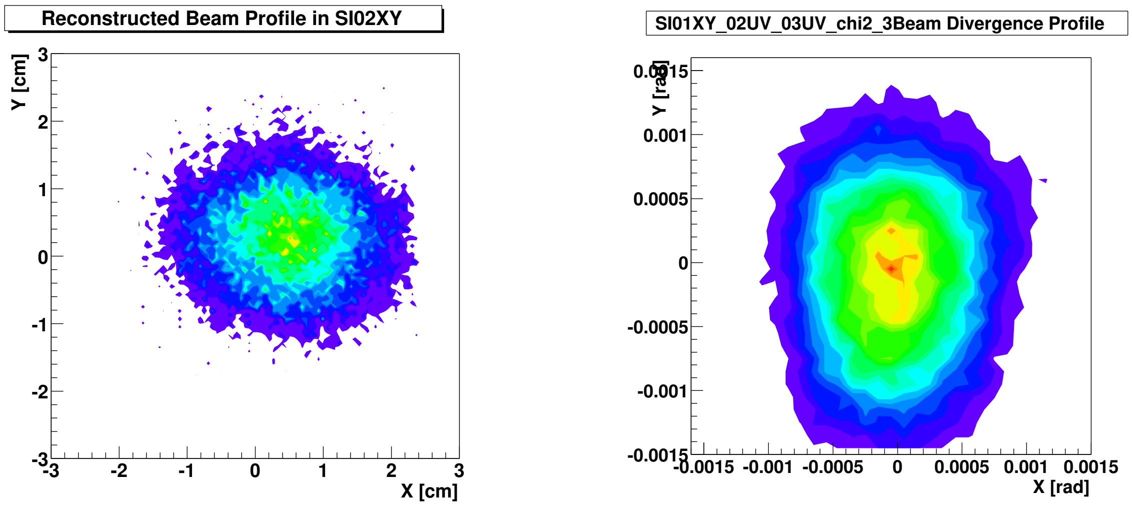

Figure 5.7: Reconstructed beam profile of silicon detector SI02XY on the left and beam divergence profile on the right of the run 31615

5.3.3 Occupancies

The occupancy is the number of hits for each strip separately, normalized to the total number of events, which is shown in figure 5.8. There is plotted the Y projection of the silicon station three during cryogenic operation at two different runs. The left graph displays a standard well shaped hit spectrum from run 32404 at $-137.7°$ C. The right one has a very noisy structure. It was taken from the run 32496 at $-141.1°$ C. This noise can be seen in all projections of the silicon detector and has the same shape. The cause of this noise could be that the APV read out chip reaches the limit of smooth operation at just this range of temperature. That indication of the temperature dependence of this noise has to be investigated with a very precise temperature scan of a silicon station at cryogenic temperature.This noise can be seen for half of the taken data. The occupancies for the runs which are discussed in this thesis are plotted in appendix C.

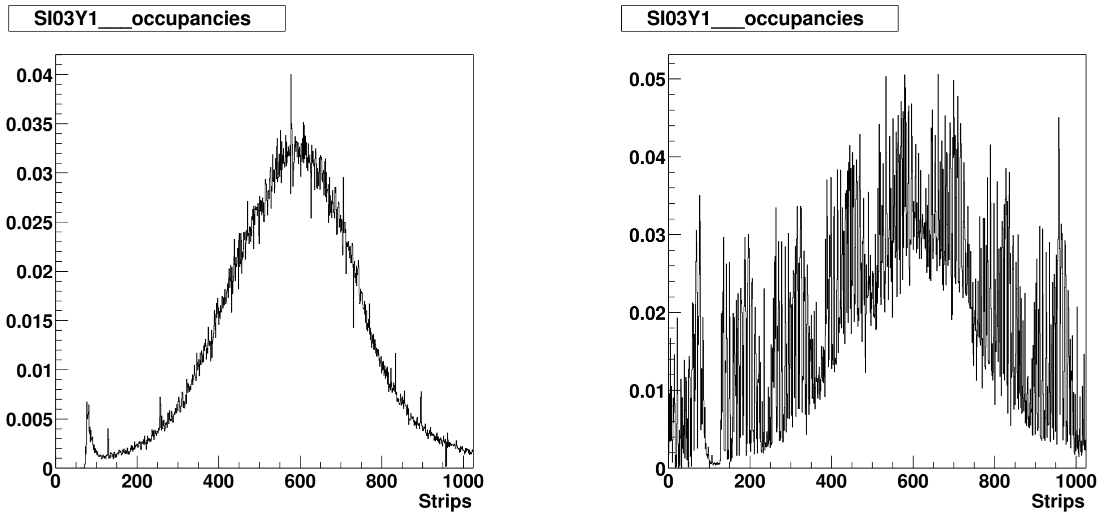

Figure 5.8: Two occupancy spectra of the Y-projection of SI03 at $-137.7°$ C on the left for run 32404, and on the right at $-141.1°$ C for run 32496

5.3.4 Cluster Size

For further analysis the cluster size plays a major role. Depending on the position where the particle is crossing the detector, the generated charge distribution is mainly seen by one or two readout strips. On the p-side (V/Y planes) of the COMPASS silicon detectors there are additional strips between the readout strips which are called intermediate strips. This intermediate strips increase the cluster size by charge division which leads to a higher spatial resolution, see chapter 5.3.5. On the n-side (U/X planes) there are no intermediate strips realized. In table 5.1 different cluster sizes are listed in percentage of the total number of clusters for a COMPASS high intensity muon (run 31615) and a low intensity 25 ns (run 32454). The values were extracted from a run analyzed with a cut on the silicon time to get rid of off-time events which are mainly noise and have a 1-strip cluster size.

The influence of the intermediate strips is seen very clear in the X/U projection only about $25-30\%$ of all clusters have cluster size two, but on the Y/V plane the ratio between cluster size one and two is roughly one. Cluster size three occurs very rarely, it is a $1-2.5\%$ effect and it is not further discussed. The third silicon station cluster size two is more often obtained compared to the first and second station. A significant effect due to cryogenic operation is not observed. In figure 5.9 is the cluster size distribution shown for the X/Y plane of the third station in warm and cryogenic operation.

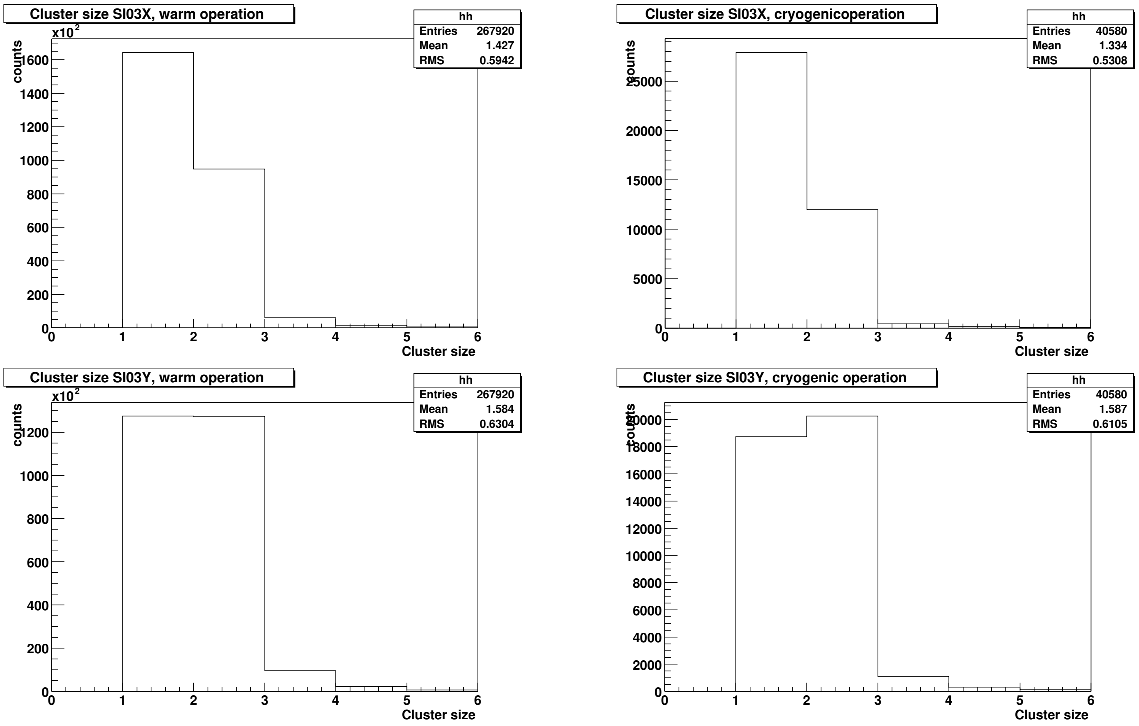

Figure 5.9: Cluster size of the silicon planes SI03X and SI03Y in warm and cryogenic operation

	Run 31615			Run 32454		
plane	cs1	cs2	cs3	cs1	cs2	cs3
SI01U	73.0	24.8	1.4	71.3	27.0	1.1
SI01V	43.7	49.5	5.0	50.8	46.2	2.1
SI01X	76.2	21.8	1.3	74.6	23.7	1.1
SI01Y	54.1	42.7	2.3	53.5	43.9	1.9
SI02U	78.0	20.2	1.0	77.7	20.7	1.0
SI02V	53.0	44.0	2.1	51.5	46.0	1.9
SI02X	66.5	31.0	1.6	65.5	32.3	1.4
SI02Y	51.8	44.4	2.7	51.2	45.7	2.3
	warm operation			cryogenic operation		
SI03U	67.5	30.2	1.5	64.1	33.5	1.3
SI03V	44.5	50.6	3.6	45.6	50.0	3.1
SI03X	61.3	35.4	2.3	68.9	29.5	1.1
SI03Y	47.6	47.5	3.6	46.3	49.9	2.7

Table 5.1: Different cluster sizes (cs) for all planes as non-trackers during COMPASS physics run (31615) and 25ns run (32454) with the third silicon station in cryogenic operation

In figure 5.10 the predicted track is plotted position modulo shifted into ten strips for cluster size one and two and the sum of both. For the U/V projection SI01UV, SI02XY, SI03XY tracked and vice versa for the X/Y projection. The plots on the left with warm operation are extracted from the run 31615 and the cryogenic ones on the right are from run 32454. The predicted track definition of a beam particle

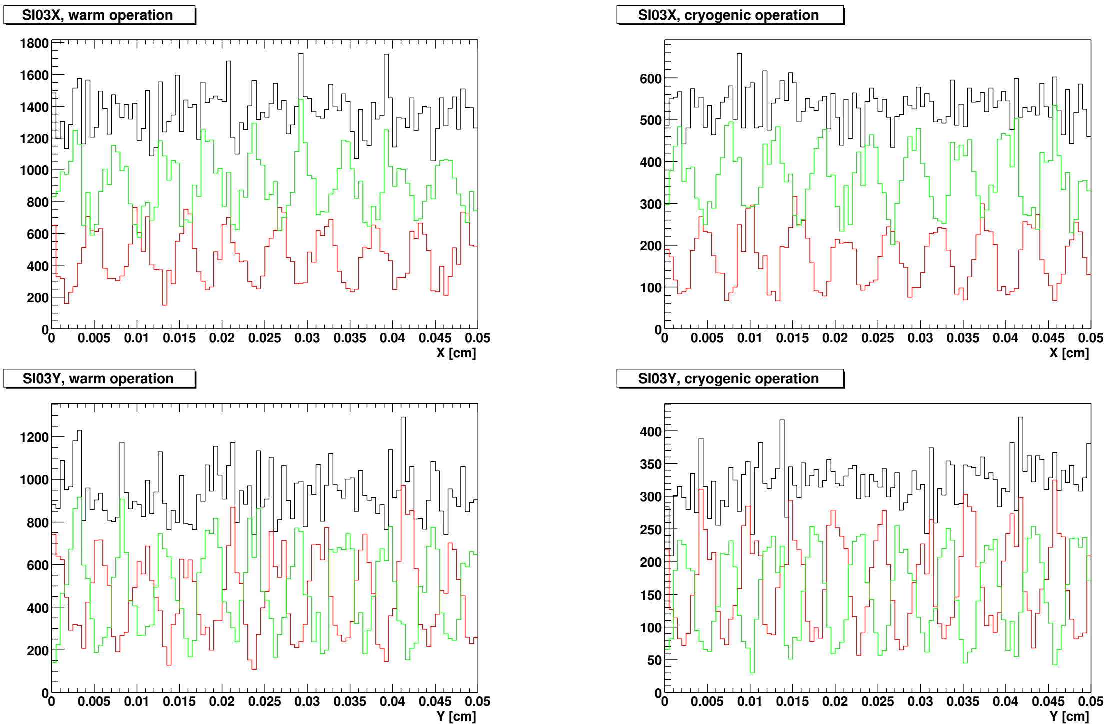

Figure 5.10: Predicted track position modulo shifted into an interval of ten strips plotted for cluster size one (green) and two (red) and the sum of both (black); on the left for warm operation and on the right for cryogenic operation of run 31615 and 32454

is the addition of the calculated position of the cluster and its residuum. The track position has to be independent of the cluster size and detector position, this can be seen (black line). The position of the signals with cluster size one (green) is expected to be distributed about the pitch and for cluster size two to have the mean of the distribution between two strips (red). This is fulfilled for all projections. For all plots a cut is made on the signal amplitude to reduce signals caused by noise. For warm operation only signal amplitudes bigger than 30 ADC channels and for cryogenic operation 50 channels were accepted. From figure 5.14 can be seen that these cuts are reasonable. This plot 5.10 is very sensitive to the pitch of the silicon. The pitch is extracted via Fourier transformation both for cluster size one and two. This values are put in the modulo shift. The position of the signals with cluster size one is expected to be distributed about the pitch and for cluster size two to have the mean of the distribution between two strips. This is fulfilled for all projections.

5.3.5 Spatial Resolution

The localization accuracy of silicon microstrip detectors depends on many different effects. Physical processes like statistical fluctuations of the energy loss and diffusion of carriers during the drift contains the first category. To a second group belong external parameters like strip and readout pitch as well as electronic noise and appropriate data analysis. Given all these constraints, a spatial resolution of 5 μm for a detector thickness of 300 μm can be achieved [Pei92].

The spatial resolution can be calculated assuming that no charge is deposited exactly on one readout strip. This value of the spatial resolution of silicon microstrip detectors is given through the width of the pitch/$\sqrt{12}$, see [Wag01]. For the silicon microstrip detector the theoretical spatial resolution is 15.781 μm (pitch 54.667 μm) on the n-side and 14.915 μm (pitch 51.667 μm) on the p-side. If more than one read out strip sees part of the charge, these adjacent strips are combined to one cluster, and the position of the cluster is calculated as the amplitude-weighted mean of the strip positions. This gives a much more precise value for the spatial resolution than the single strip information discussed above.

In order to determine the spatial resolution, a precise alignment and reliable tracking is necessary. For this it is useful to have a look at the residuals versus the position in the detector. If the geometry of the silicon detector is given correctly, the residuals should be distributed around zero along the whole silicon detector. The relative position and rotation of the detector planes can be calibrated this way, and this was in fact a major part of the present work in order to obtain the spatial resolution. As presented in fig 5.11 the third silicon station in cryogenic operation shows a rotation, with respect to the warm position. For the particular cryogenic runs the silicon detectors of the third station station have to be aligned by rotating them about a certain angle a round the z-axis. For the SI03UV silicon detector the maximum rotation for different runs was 0.8 mrad, for the other detector 1.6 mrad in Y and 3.0 mrad in X. Although not yet understood in detail, it is obvious that the different thermal expansion coefficients of single components like PCB, silicon glue and silicon wafer the whole distorts.

On the further way to determine the spatial resolution, the relations depending on the cluster size between the width of the residual, the spatial resolution of the detector, the errors of the track and the effects of multiple scattering are discussed. The tracking is investigated here with two configurations with three out of six silicon detectors active SI03XY, SI01UV, SI02XY, or SI03UV, SI02XY, SI03XY, respectively, the three other stations passively. Since the three silicon stations are placed very symmetrically, except of little shifts of 2 cm and 4 cm, the behavior can be explained in a simplified model, which further assumes that only two orthogonal projections are measured namely the $x - z$ plane; for the $y - z$ plane the situation is analogue. The U projection can be seen as a linear combination of x and y with 99% proportion in x, the stereo angle of 5° serves mainly for resolving multi-hit ambiguity, which is not discussed here.

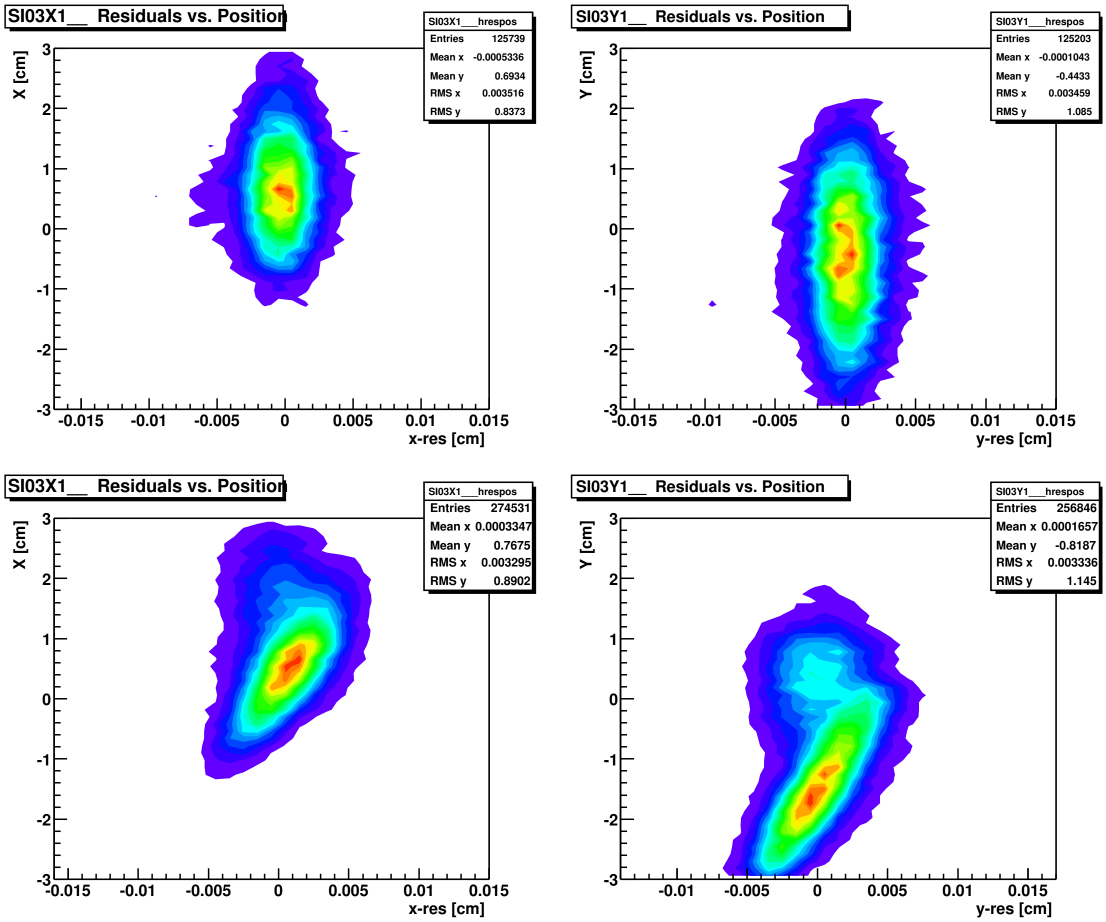

Figure 5.11: The residual versus detector position of SI03 X and Y projection in run 31615 during warm operation (the upper plots) and run 32454 in cryogenic operation. The distortion of the detector in cryogenic operation can be seen very obviously.

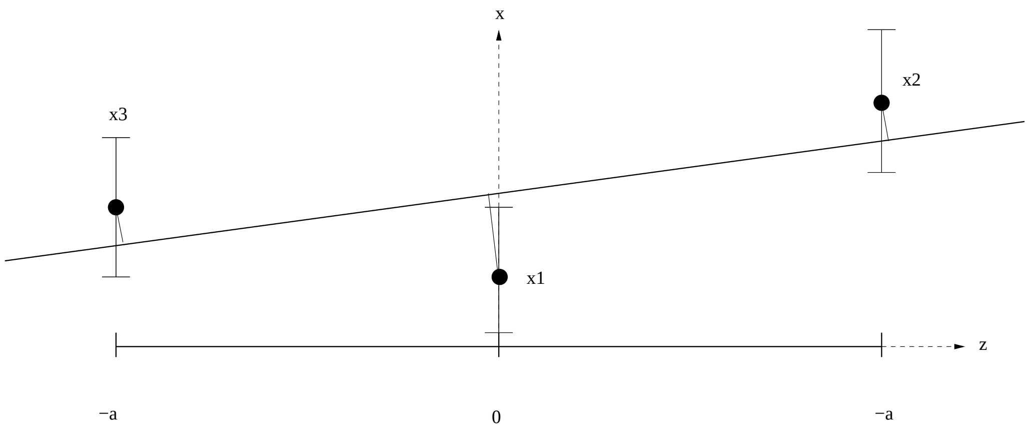

Figure 5.12: Sketch for a simple model to understand the residual width

Assuming the detector positions at $z_1 = -a, z_2 = 0, z_3 = a$ three measured points $(-a, x_3), (0, x_1), (a, x_2)$, see figure 5.12, fitted with a straight line

$$x_i = a + bz_i, \tag{5.1}$$

gives, the χ^2- minimizing fit parameters assuming the same resolution for all three points,

$$a = \frac{x_3 + x_1 + x_2}{3} \quad \text{and} \quad b = \frac{x_2 - x_3}{2a}. \tag{5.2}$$

The residual res_1 is the spacing of the x_1 to the fit:

$$\mathrm{res}_1 = x_1 - \left(\frac{x_3 + x_1 + x_2}{3}\right) = -\frac{x_3}{3} + \frac{2x_1}{3} - \frac{x_2}{3}. \tag{5.3}$$

Further res_2 is calculated by

$$\mathrm{res}_2 = x_2 - \left(\frac{x_3 + x_1 + x_2}{3} + \frac{x_2 - x_3}{2a} \cdot (-a)\right) = \frac{x_3}{6} - \frac{x_1}{3} + \frac{x_2}{6}, \tag{5.4}$$

for res_3 it is equal to res_2. It can be seen that

$$\mathrm{res}_1 = -2 \cdot \mathrm{res}_2 = -2 \cdot \mathrm{res}_3. \tag{5.5}$$

The width of the residual is given by the error propagation of the track error. In general the error propagation can be calculated with the covariance matrix applied to a vector **a** in the following way:

$$\mathrm{cov(x)} = \mathbf{a}^{\mathbf{T}} \mathrm{cov}(x_0) \mathbf{a} \tag{5.6}$$

This calculation is explicitly done for this particular configuration.

$$\delta^2_{\mathrm{res}_1} = \begin{pmatrix} -\frac{1}{3} \\ \frac{2}{3} \\ -\frac{1}{3} \end{pmatrix}^T \begin{pmatrix} \sigma_3^2 & 0 & 0 \\ 0 & \sigma_1^2 & 0 \\ 0 & 0 & \sigma_2^2 \end{pmatrix} \begin{pmatrix} -\frac{1}{3} \\ \frac{2}{3} \\ -\frac{1}{3} \end{pmatrix} \overset{\sigma_i = \sigma_j}{=} \frac{2}{3} \sigma^2_{\mathrm{det}} \tag{5.7}$$

The σ for each detector plane is assumed to have the same value. For the residual width δ of the tracking detector the following relation with the detector resolution follows:

$$\delta_{\mathrm{res}_1} = \sqrt{\frac{2}{3}} \cdot \sigma_{\mathrm{det}} \approx 0.817 \cdot \sigma_{\mathrm{det}} \tag{5.8}$$

$$\delta_{\mathrm{res}_2} = \sqrt{\frac{1}{6}} \cdot \sigma_{\mathrm{det}} \approx 0.408 \cdot \sigma_{\mathrm{det}}. \tag{5.9}$$

$$\tag{5.10}$$

The correct estimation of the spatial resolution σ_{det}, which is an input parameter for the fit is seen also in a flat χ^2 probability distribution, assuming other effects like multiple scattering to be small. In the following σ_{det} will be called σ_{as} because it is the assumed spatial resolution and input parameter for analysis with COOOL and simulations of the tracking.

The next step is to have a look at the non tracking silicon detectors. Their residual σ_{det} is the deconvolution of the measured residual width σ_{meas} of the silicon detector and the error of the track σ_{track}:

$$\sigma_{\text{det}}^2 = \sigma_{\text{meas}}^2 - \sigma_{\text{track}}^2 \tag{5.11}$$

The so determined spatial resolution σ_{det} should have the same value like the assumed input spatial resolution of the tracking σ_{as} and serves as a cross check. To get σ_{det} the error of the track σ_{track} has to be determined in consideration of effects of multiple scattering.

Multiple Scattering For the multiple scattering the radiation lengths of all material which affects the beam particle has to be estimated. If a particle passes the three detectors the scattering effect can be assumed for the third station. If there was no multiple scattering, particles would follow a straight line. Scattering effects at the first detector cannot be seen because there is no information of the track before the first detector, also scattering at the third detectors, see figure 5.13. The effects in between are mainly given by the material of the second station. In the worst case the beam particle is affected by the two silicon detectors ($2 \times 3.2 \cdot 10^{-3}$ R.L.), air ($2.2 \cdot 10^{-3}$ R.L.), two layers of mylar foil of the detector window ($2 \times 8.7 \cdot 10^{-5}$ R.L.) and eventually some of two Kevlar yarns ($2 \times 1.4 \cdot 10^{-3}$ R.L). The scattering, mostly due to multiple Coulomb scattering is for small deflection angles roughly Gaussian for the central 98% of the projected angular distribution with a width [PDG00]

$$\theta_0 = \frac{13.6\,\text{MeV}}{\beta c p} z \sqrt{x/X_0} \cdot [1 + 0.0038 \ln(x/X_0)]. \tag{5.12}$$

Here are cp the muon energy of 160 GeV, β can be set to one, z is the charge number of the incident muon, x/X_0 the thickness of the scattering medium in radiation lengths, in varies between $11.6 \cdot 10^{-3}$ $8.8 \cdot 10^{-3}$ depending on how much Kevlar yarn is hit. It follows an angle θ_{max} is about $7.6 \cdot 10^{-6}$ µrad. That translates at the distance between the second and third detector (≈ 63 cm) to a deflection of 4.8 µm. The probability that all Kevlar yarns are hit is very little, because more than 95% of the detector windows are only mylar foil. In the best case no Kevlar is hit and the θ_{best} is $6.5 \cdot 10^{-6}$ µrad with 4.1 µm deflection. This deflection σ_{mult}

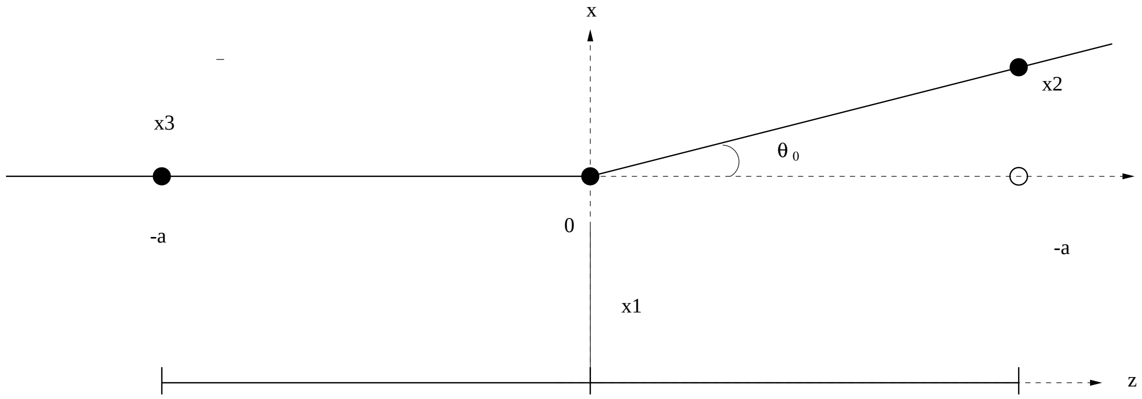

Figure 5.13: Draft of the setup for the theoretical understanding of multiple scattering by tracking with three detectors

has to be added quadratically to the assumed spatial resolution σ_{as} of the detector to get the total uncertainty

$$\sigma_{\mathrm{as+mult}} = \sqrt{\sigma_{\mathrm{as}}^2 + \sigma_{\mathrm{mult}}^2} \tag{5.13}$$

The effects of multiple scattering are studied by a simulation. The localization of a particle in the detector is not absolute but Gaussian distributed with the sigma of the spatial resolution. This is simulated with random values Gaussian distributed with the assumed spatial resolution of the three tracking detector positions. Through this simulated data a straight line fit is done and the residuals are calculated. The covariance matrix of the straight line fit delivers the error of the track σ_{track}. To take multiple scattering (best case)into account in the simulation the $\sigma_{\mathrm{as+mult}}$ was used for the third detector in beam direction instead of σ_{as}. For the fit the estimated values σ_{as} were used. The simulation shows that multiple scattering broadens the residuals about $0.1 - 0.2$ µm and has only very little effect.

Results The spatial resolution is analyzed in detail for run 32454, which was taken during the 25 ns period and the third station was in cryogenic mode. The main observation is the very strong dependency of the spatial resolution on the cluster size of the detector. The track error σ_{track} including the multiple scattering is calculated for all eight combinations of cluster size 1 or 2 of the three tracking detectors by the simulation. The sigma of the measured residual σ_{meas} is determined in cuts of the cluster size configuration of the trackers and the cluster size of the analyzed plane, see table 5.2. It is estimated that the deconvolution of σ_{meas} with σ_{track} is always the same value σ_{det} which should be equal to σ_{det}. But it is observed that if the neighbor tracker has cluster size 1 the spatial resolution σ_{det} is $1-3$ μm for X and U projection and $4-5$ μm in V and Y projection higher that the σ_{det} is if the neighbor tracker has cluster size 2. This can be explained that the positions for cluster size one are quantized values, but for the analysis Gaussian distribution was assumed which is not correct for this case. The assumed resolutions σ_{as} are consistent with the σ_{det} if one neighbor tracker has cluster size 2, except of U and X plane with cluster size 2 the sigma was estimated too small in the analyzed detector. In general the spatial resolution of SI01 is worse than the other two stations. Due to the fact that all detectors have the same wafer design and the spatial resolution should be the same for all stations. It has to be investigated if this is connected to the to radiation damage. The spatial resolution on the Y and V projection is better than on the X and U plane due to the intermediate strips on the p-side, which is consistent with the detector design. In Y/V projections, an excellent resolution $\sigma_{\text{det}} \approx 4$ μm is reached for 2-strip cluster size.

		neighbor tracker cluster size 1			neighbor tracker cluster size 2			
plane	cs	σ_{meas}	σ_{track}	σ_{det}	σ_{meas}	σ_{track}	σ_{det}	σ_{as}
SI01U	1	16.4 15.8 15.5 15.2	7.5 6.6 6.5 5.2	**14.4 ± 0.2**	14.3 13.7 13.6 13.9	6.0 5.6 5.5 4.6	**12.8 ± 0.3**	13
	2	14.2 12.6 12.8 11.7		**11.5 ± 0.6**	11.6 11.7 12.3 11.0		**10.3 ± 0.5**	8
SI01V	1	13.3 14.9 14.0 14.5	5.2 4.4 4.2 2.7	**13.9 ± 0.5**	10.0 9.7 10.0 10.6	3.4 3.1 3.1 2.3	**9.6 ± 0.4**	9
	2	13.1 13.5 12.6 12.7		**12.3 ± 0.3**	6.4 7.3 7.3 8.6		**6.7 ± 1.0**	4
SI01X	1	17.1 16.4 16.6 15.2	7.5 6.7 6.5 5.2	**15.1 ± 0.3**	15.4 14.2 14.2 14.3	6.1 5.7 5.5 4.6	**13.6 ± 0.5**	13
	2	14.5 14.3 13.9 12.1		**12.3 ± 0.5**	12.1 11.1 11.7 10.0		**10.1 ± 0.5**	8
SI01Y	1	15.8 15.1 15.3 14.6	5.2 4.5 4.2 2.7	**14.6 ± 0.2**	10.2 10.6 10.8 11.0	3.4 3.2 3.0 2.3	**10.2 ± 0.4**	9
	2	13.1 12.8 13.0 13.0		**12.2 ± 0.3**	6.2 7.1 7.7 8.9		**6.8 ± 1.2**	4
SI02U	1	19.4 19.0 18.5 17.9	12.0 11.3 11.9 10.8	**15.0 ± 0.4**	15.3 15.3 14.9 14.3	7.7 7.5 7.7 7.4	**13.0 ± 0.3**	13
	2	16.7 15.8 16.1 16.9		**11.6 ± 0.7**	13.1 12.0 12.5 12.8		**10.1 ± 0.5**	8
SI02V	1	14.5 15.1 13.2 16.6	8.3 7.5 8.2 6.6	**12.6 ± 1.7**	9.4 9.5 9.2 9.2	3.9 3.8 3.9 3.7	**8.5 ± 0.1**	9
	2	11.8 14.1 12.0 15.4		**9.5 ± 1.7**	6.0 5.9 5.4 6.6		**4.4 ± 0.4**	4
SI02X	1	18.5 17.4 18.0 16.9	12.0 11.1 11.8 10.7	**13.8 ± 0.3**	15.3 14.5 14.1 14.5	7.7 7.5 7.7 7.3	**12.7 ± 0.6**	13
	2	15.3 14.9 15.4 14.6		**9.8 ± 0.2**	12.1 9.8 13.3 16.1		**10.4 ± 2.6**	8
SI02Y	1	14.6 15.2 14.4 15.6	8.2 7.3 8.1 6.5	**12.7 ± 0.9**	9.8 9.3 8.9 9.7	3.9 3.8 3.9 3.7	**8.6 ± 0.5**	9
	2	11.4 13.6 11.2 14.2		**8.9 ± 1.7**	5.4 5.7 5.4 6.2		**3.9 ± 0.4**	4
SI03U	1	20.4 19.8 19.2 18.1	11.7 10.7 11.6 10.2	**16.3 ± 0.7**	16.7 15.8 15.9 16.1	7.7 7.3 7.6 7.1	**14.5 ± 0.4**	13
	2	16.6 16.7 16.7 15.3		**12.0 ± 0.5**	13.5 12.7 13.6 12.5		**10.8 ± 0.4**	8
SI03V	1	14.7 15.9 14.4 15.9	8.1 6.9 8.0 6.1	**13.2 ± 1.1**	9.9 9.8 9.9 9.6	3.9 3.8 3.9 3.6	**9.0 ± 0.1**	9
	2	11.4 13.4 11.2 14.3		**9.0 ± 1.6**	6.6 6.7 6.8 7.3		**5.5 ± 0.2**	4
SI03X	1	19.1 17.8 17.3 17.8	11.8 10.9 11.7 10.4	**14.5 ± 0.8**	15.5 15.1 15.1 14.2	7.7 7.4 7.7 7.3	**13.3 ± 0.3**	13
	2	16.1 16.2 17.6 15.8		**12.0 ± 0.9**	12.9 12.7 13.6 13.3		**10.7 ± 0.4**	8
SI03Y	1	15.2 16.9 15.0 18.1	8.1 7.1 8.1 6.2	**14.1 ± 1.7**	9.1 9.7 9.3 9.5	3.9 3.8 3.9 3.6	**8.5 ± 0.3**	9
	2	11.4 15.0 12.3 16.1		**10.0 ± 2.4**	6.3 6.7 6.4 7.4		**5.2 ± 0.4**	4

Table 5.2: Run 32454: For the planes of non tracking silicon detectors with cluster size (cs) one or two is for the residual σ_{meas} determined cut on each combination of the cluster sizes in the tracking detectors (divided in column neighbor cluster size 1 and 2 and there the four possible cluster size combinations 1-1, 1-2, 2-1, 2-2 for the other trackers are given and the track error as well); σ_{meas} is deconvoluted with the corresponding track error σ_{track}, for these four combination the average spatial resolution σ_{det} is given; σ_{as} is the assumed resolution.

In table 5.3 are shown the residual widths σ_{meas} for the silicon planes taking part in the tracking and for both cases cluster size one and two for all trackers. Compared with the expected width of the simulation σ_{meas} is for all planes too big. For cluster size one the quantized values for the cluster position can be responsible for this effect. Up to now the the 5° degree of the U and V plane compared to the X an Y is not taken into account and its effects.

	cluster size 1		cluster size 2	
plane	σ_{meas}	σ_{exp}	σ_{meas}	σ_{exp}
SI01U	14.4 ± 0.1	10.6	9.8 ± 0.1	6.6
SI01V	13.2 ± 0.1	7.5	7.3 ± 0.1	3.6
SI01X	14.3 ± 0.1	10.6	9.2 ± 0.2	6.6
SI01Y	12.8 ± 0.1	7.5	6.8 ± 0.1	3.6
SI02U	7.1 ± 0.1	5.0	4.5 ± 0.1	3.1
SI02V	6.9 ± 0.1	3.5	3.8 ± 0.1	1.7
SI02X	6.8 ± 0.1	5.0	4.4 ± 0.1	3.1
SI02Y	6.5 ± 0.1	3.5	3.7 ± 0.1	1.7
SI03U	7.8 ± 0.1	5.7	4.8 ± 0.1	3.5
SI03V	7.0 ± 0.1	4.0	4.6 ± 0.1	1.9
SI03X	7.8 ± 0.1	5.7	5.0 ± 0.1	3.5
SI03Y	7.4 ± 0.1	4.0	5.0 ± 0.1	1.9

Table 5.3: Residual widths σ_{meas} for silicon planes taking part in the tracking for both cases cluster size one and two for all trackers; σ_{exp} is the expected residual width of the tracker inclusive multiple scattering

5.3.6 Amplitude

The amplitude signal of the silicon detectors of station three show the characteristic Landau distribution. In figure 5.14 there are shown the amplitudes of all four projections of the third silicon station for warm and cryogenic operation. The runs 31615 and 32454 are analyzed with a cut on the silicon time to reject off time events which are mainly due to noise. The last two plots are created without this time cut and signals with amplitudes lower 30 ADC channels are four times more often. That means the cut on the silicon time is really sufficient. The black curve is the amplitude signal and the green one represents the amplitude signal for cluster size one and the red one for cluster size two. The ratio of both cluster sizes depending on the projection can be seen very clear. The noise signals with amplitudes less than 10 ADC channels are suppressed by the frontend electronic and not stored. For cluster size two signals with low amplitudes are less probable for the U/X projection because of the missing intermediate strips. The rise to higher amplitudes for signals with cluster size two can be explained that for signals with high amplitudes the collection charge distribution is wider and it is more probable to spread over two strips. Both effects are observed for warm and cryogenic operated silicon. The great difference between these two operating conditions are the increase of the mean value of the amplitude distribution approximately 15%. This effect can be explained mainly of the changed behavior of the APV chip. In cryogenic operation the preamplifier of the APV chip changes its time evolution the signal rises faster and increases its amplitude.

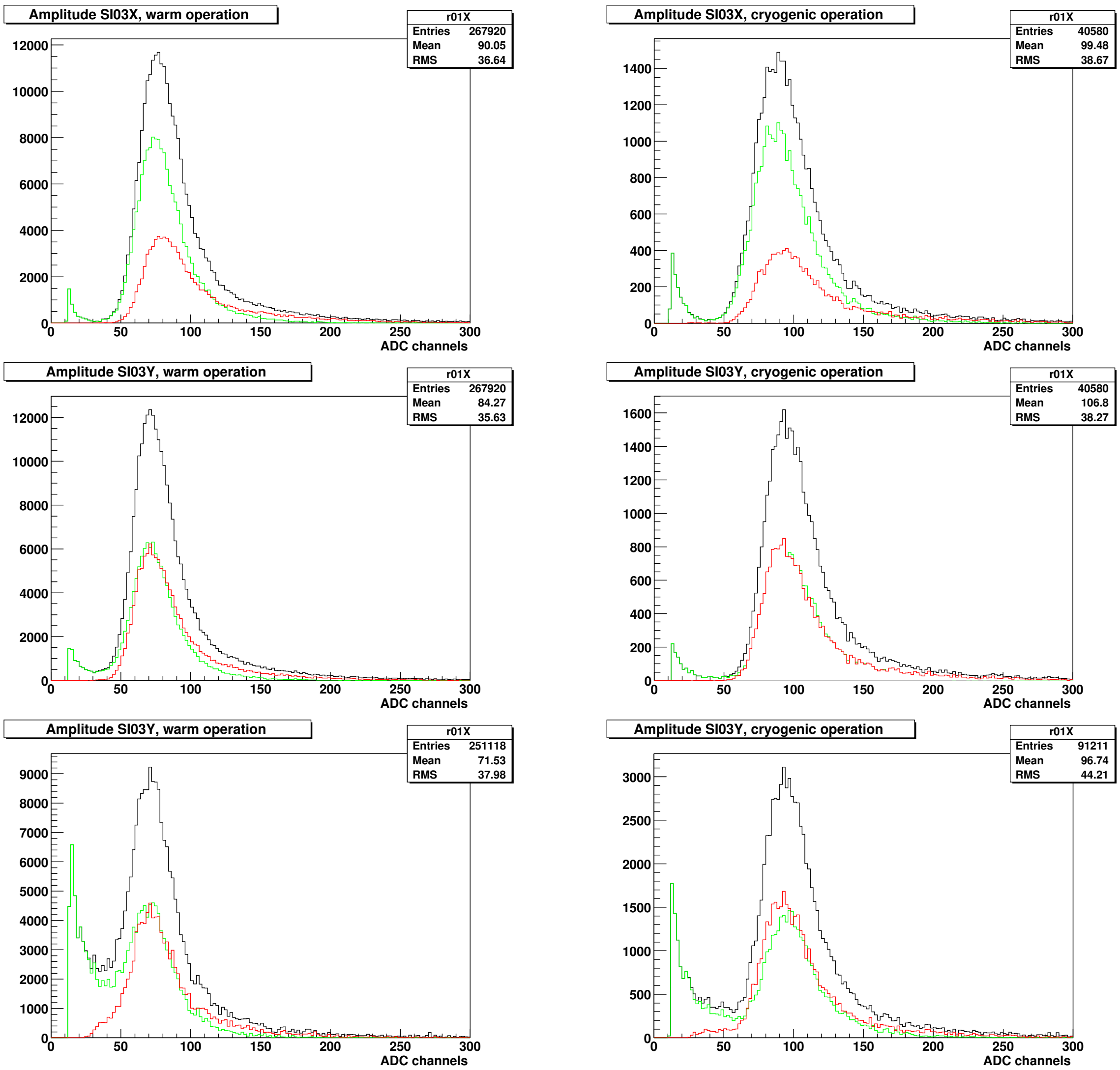

Figure 5.14: There displayed the signal amplitude distribution for the X and Y plane of the third silicon station with silicon time cut 15 for warm and cryogenic operation. The two last plots are made without a silicon time cut.

5.3.7 Signal to Noise Ratio

During the 25 ns beamtime also data with electron beam were taken, both with cryogenic and warm operation. Due to the low intensity of this beam it was possible to run the APV readout chips in latch all mode. That means, all channels of the silicon detector are read out without any noise suppression. The latch all data were analyzed with the gemMonitor written by Bernhard Ketzer [Ket01].

In figure 5.15 is displayed a bias scan of the signal to noise ratio of the third silicon station, both for warm and cold operation. The data were taken with physics and random trigger to be able to reconstruct the pedestals of the APV chips. The nominal voltage of the third silicon station XY-projection was 50 V this beamtime. As noise reference were taken the sigma of the common mode noise corrected baseline level of the fifth APV chip of each detector side. It can be observed, that the increase of the signal compared to the noise is about 50%. The major responsible effect is the changed behavior of the APV chips preamplifier. For the bias scan in warm operation can easily seen the decrease of the signal to noise ratio with lower bias voltage. This is the expected effect because the silicon is not fully depleted any longer. But in cryogenic operation the signal to noise ratio is constant over the whole scan. An explanation is the increase of the mobility of charge carriers which makes the silicon detector fully depleted at lower bias voltage.

5.3.8 Time Resolution and Efficiency

The time resolutions of all planes of the silicon station SI03 for warm and cryogenic operation are summarized in table 5.4. As can be seen a silicon detector at cryogenic temperature has excellent time resolutions. It is also observed that the cluster size has an effect on the time resolution. For 2-strip cluster size events have approximately a 10% lower time resolution than events with cluster size one. There is a difference noticed in the time resolution between the p- (U/X) and n-side (V/Y) of the detector. The reason of this behaviour has still to be investigated. In figure 5.16 is displayed the time resolution of the X-plane of silicon station SI03 for both operation modes as example.

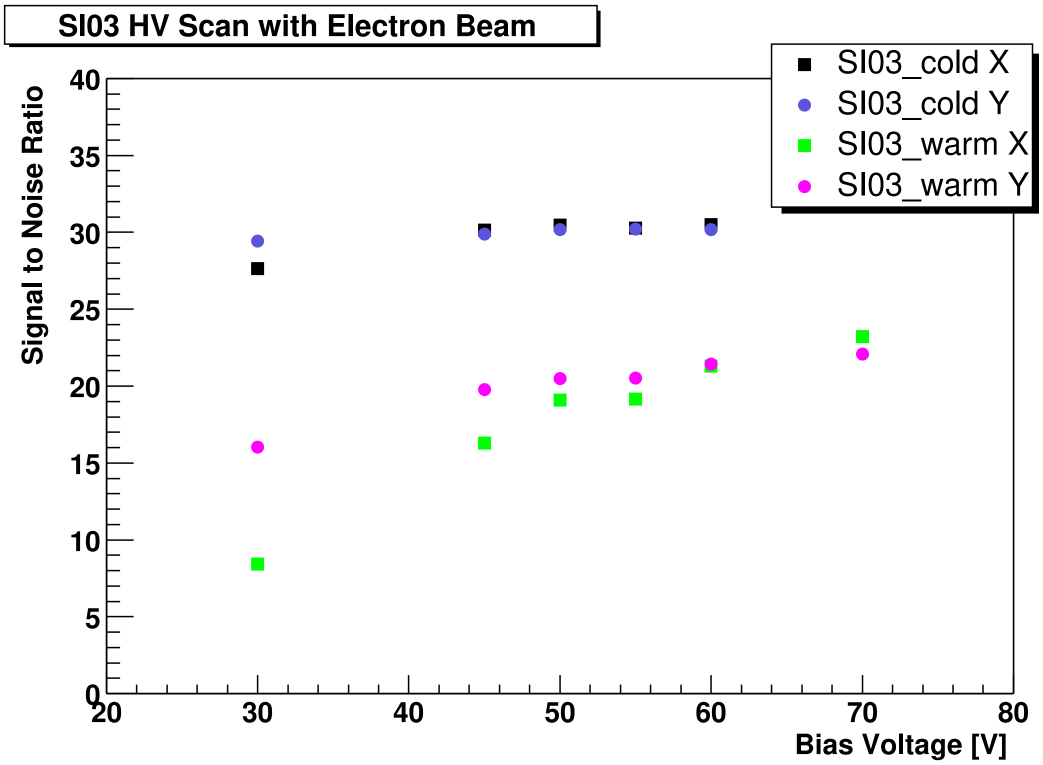

Figure 5.15: Bias scan of the signal to noise ratio of Si03 X (n-side) and Y (p-side) projection for warm and cryogenic operation

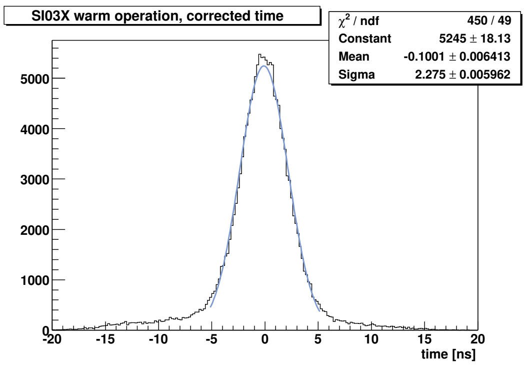

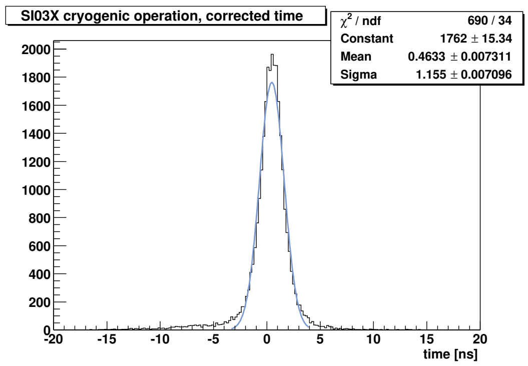

Figure 5.16: Time resolution of SI03X for warm and cryogenic operation with 1-strip cluster size, the non Gaussian tails are attributed to the pile up, that deviates the amplitude and timing information.

warm operation		
plane	cs 1	cs 2
SI03U	2.33 ± 0.01	2.40 ± 0.01
SI03V	3.43 ± 0.01	3.89 ± 0.01
SI03X	2.28 ± 0.01	2.47 ± 0.01
SI03Y	3.89 ± 0.01	4.25 ± 0.01
cryogenic operation		
SI03U	1.60 ± 0.01	1.90 ± 0.02
SI03V	1.51 ± 0.01	1.57 ± 0.01
SI03X	1.16 ± 0.01	1.24 ± 0.01
SI03Y	1.46 ± 0.01	1.61 ± 0.01

Table 5.4: Time resolution of the silicon station SI03 in the warm (run 31615) and cryogenic operation (32454) for both 1-strip and 2-strip cluster size, this is the result of a fit with a Gaussian to the distribution in figure 5.16 can be seen the non Gaussian tails.

Efficiency is the ratio of the seen tracks in the detector and the number of tracks that crossed the detector. A reliable efficiency determination depends strongly on the purity of the track reconstruction. Fake tracks, due to noise or off-time events, can be prevented with multi-hit ambiguity resolving, which is done using the 5° stereo angle between the X/U planes. The purest tracking is obtained with all other detectors active except the one whose efficiency is to be determined, which means a single configuration for each plane. Due to time constraints, this work could not be finished in this analysis so far. A first look at the efficiencies did not show, however, a significant difference between warm and cryogenic operation and for a different bias voltage. In the following figures sample efficiency maps are shown. In figure 5.17 can be seen the beam profile, which may indicate that the track sample was not purified. The values of $92.9 - 97.4\%$ should hold at least as lower limits for the real efficiencies.

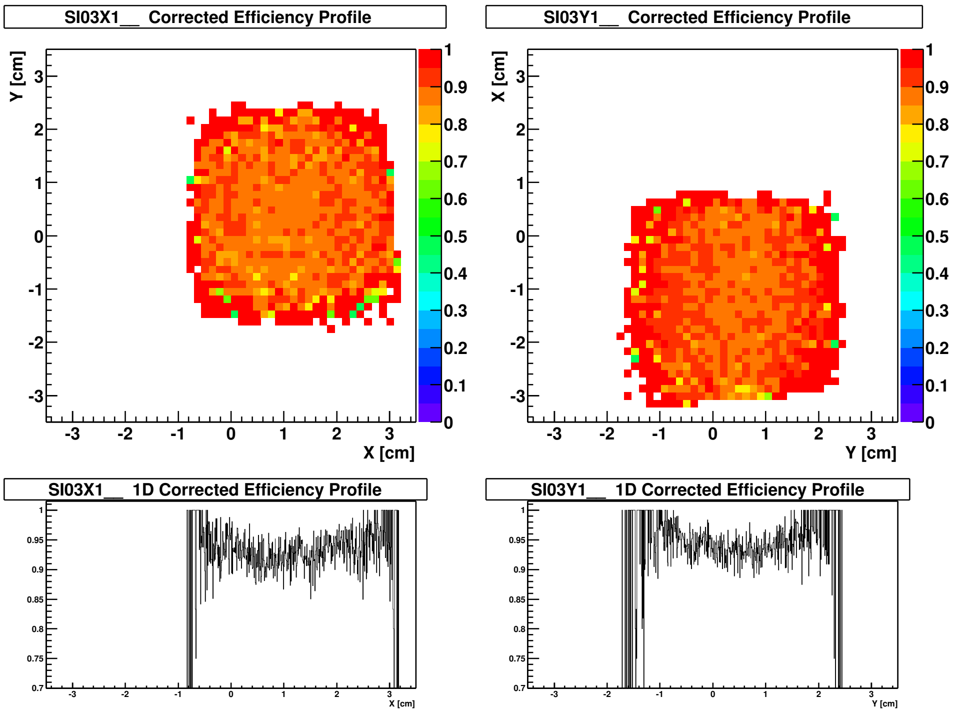

Figure 5.17: Preliminary Efficiency of SI03XY for run 31615. Average values 92.9% in X and 94.0% in Y at 50 V and warm operation.

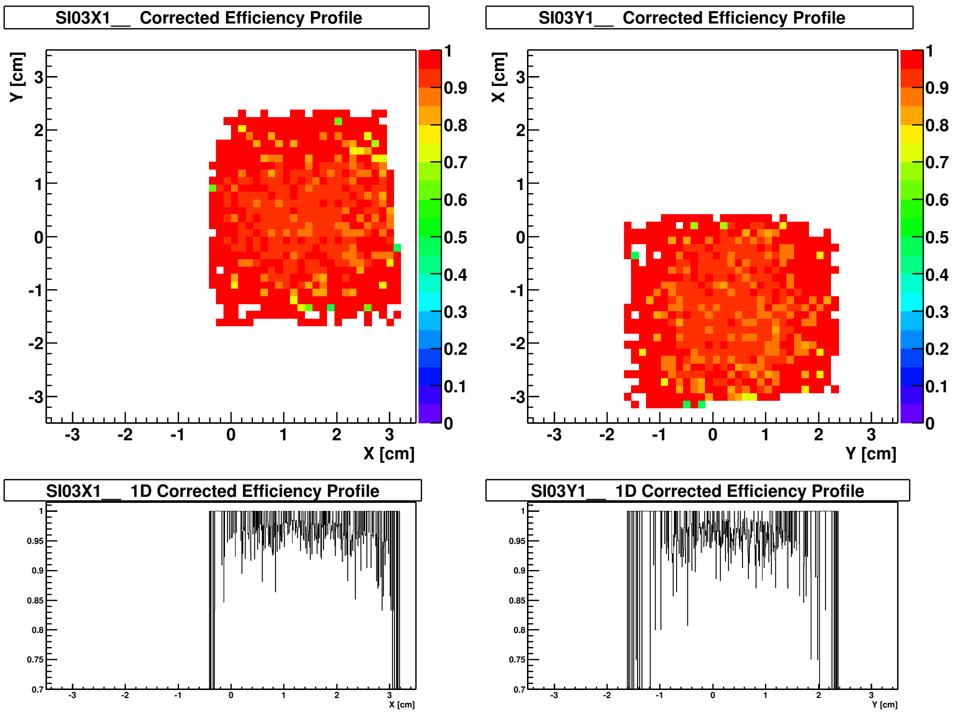

Figure 5.18: Preliminary Efficiency of SI03XY for run 32454. Average values 97.4% in X and 96.4% in Y at 50 V and cryogenic operation.

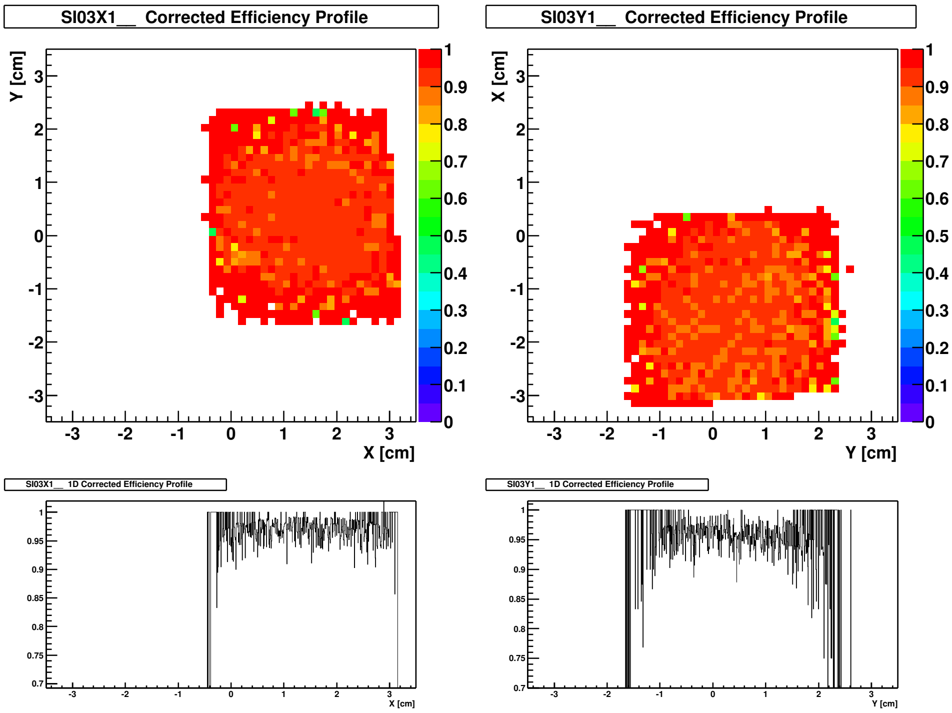

Figure 5.19: Preliminary Efficiency of SI03XY for run 32496. Average values 97.2% in X and 95.8% in Y at 30V and cryogenic operation.

Chapter 6

Conclusion and Outlook

The major modification within the mark of this thesis, in order to go from warm to cryogenic operation of a silicon detector, is the development of a new vacuum and light tight detector window, made of a Kevlar yarn support construction and on the flange clamped mylar foil. It shows a good performance, a high-vacuum approximately $4 \cdot 10^{-5}$ mbar which corresponds to the limits of the setup. Several tests were done which lead to the result that there exists potential to reduce the average mass density from 11.48 mg/ cm^2 to 6.73 mg/ cm^2.

For the COMPASS beamtime 2003, three silicon stations were installed. One station was equipped for cryogenic operation. It was proven that cooling and operating a silicon detector with liquid nitrogen at 130 K is possible. However, it was observed that the laboratory setup at CERN is a short time solution and a stable operation over several days is not possible. Apart from that some parts of the setup have to be reengineered or modified, like the nitrogen outlets and connections to the vacuum pump with bigger diameter. Further developments have to be made for the installation of the nitrogen distribution box next year at CERNṪherefore the CERN TIS approval has to be achieved.

This beamtime the leakage current of the silicon detectors was monitored for the first time due to new HV modules. The increase of the leakage current was of about a factor of 2 at the silicon stations SI01/02 and about a factor of 3 at the new silicon station SI03. To analyze the behavior of silicon detectors which get damaged due to radiation in more detail, it is necessary to integrate the HV modules to the COMPASS slow control, such that the data is stored in a data base.

In the analysis part, the first step was made up by alignment calibrations in order to get a good tracking. It is observed that in cryogenic operation the silicon detectors showed a distortion and had to be realigned for each particular run. A significant difference of the cluster size of a silicon detector in warm or cryogenic operation is not observed. The spatial resolution of the silicon detectors is strongly dependent on the cluster size of the analyzed detector and its neighbor tracker. In general the 2-strip clusters show a better resolution. The spatial resolutions have been determined to be for 1-strip cluster size $12.8 - 14.5$ μm in (U/X) plane, $8.5 - 10.5$ μm (V/Y), for 2-strip cluster size $10.1 - 10.8$ μm in (U/X), $3.9 - 6.9$ μm (V/Y). It is also observed that the signal amplitude is of about 15% higher in cryogenic operation due to the changed behavior of the APV readout chip. The occupancy spectra for a cooled silicon detector show a very noisy structure. It seems that at a temperature of around 130K the limits of the APV chip are reached. This has to be validated with a precise temperature scan.

The time resolution of the silicon detectors in warm operation also show a dependence of the cluster size and the particular detector plane, 2.3 ns in (U/X), approximately 3.5 ns in (V/Y) for cluster size one. For 2-strip cluster size the values are 10% higher. For cryogenic operation, the time resolution is about a factor of two better than in warm operation, in the order of 1.5 ns. The reason of all these dependencies are under investigation.

The efficiency depends strongly on the purity of the track reconstruction. A first look at the efficiencies did not show a significant difference between warm and cryogenic operation, and preliminary efficiency maps are shown.

There is huge amount of data left which has to be analyzed like a bias and latency scan for cryogenic operated silicon as well as a bias scan with electron beam and the APV chip in latch all mode, which means that all channels are readout without zero suppression, which is very useful to study the noise behavior.

Appendix A

Detector Window

A.1 Components Used for the Detector Window

- $284 \times 284 \times 10$ mm^3 aluminum plate
- O-ring produced by PARKER O-Ringe PARKER Nr.2-176 (inner diameter: 234.62, outer diameter: 239.86)
- KEVLAR yarn produced by Du Pont, test piece KEVLAR yarn splitted into four yarns of either, 0.16 g/ m, 0.26 g/ m
- Mylar foil of mass density of 1.39 g/ cm^3, used foils of 25 μm and 12 μm thickness, metalized by 14 nm aluminum layer and 25 μg/ cm^2
- $254 \times 210 \times 5$ mm^3 aluminum flange with an opening 206×162 mm^2

A.2 Engineering Drawings of the Detector Window

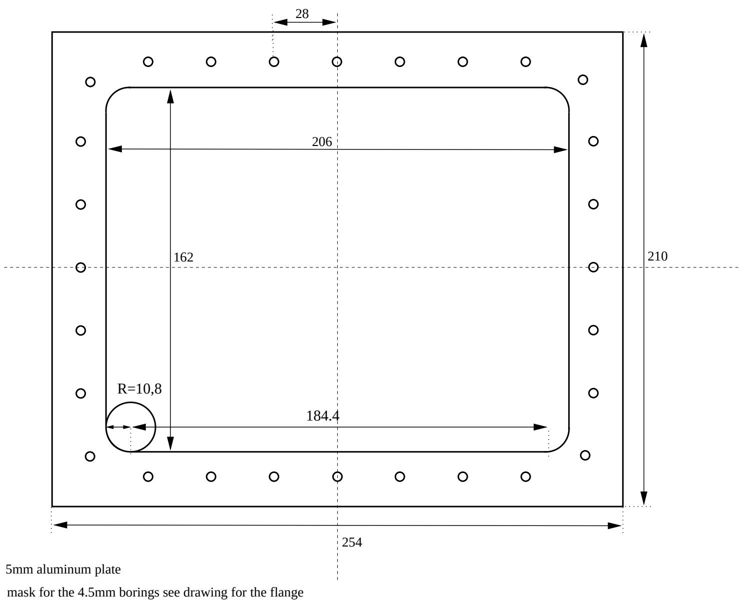

Figure A.1: Flange of the detector window

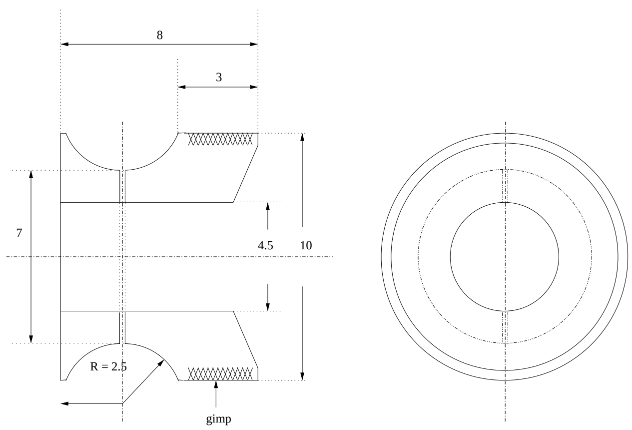

Figure A.2: Knurled screw used to fix the Kevlar yarn

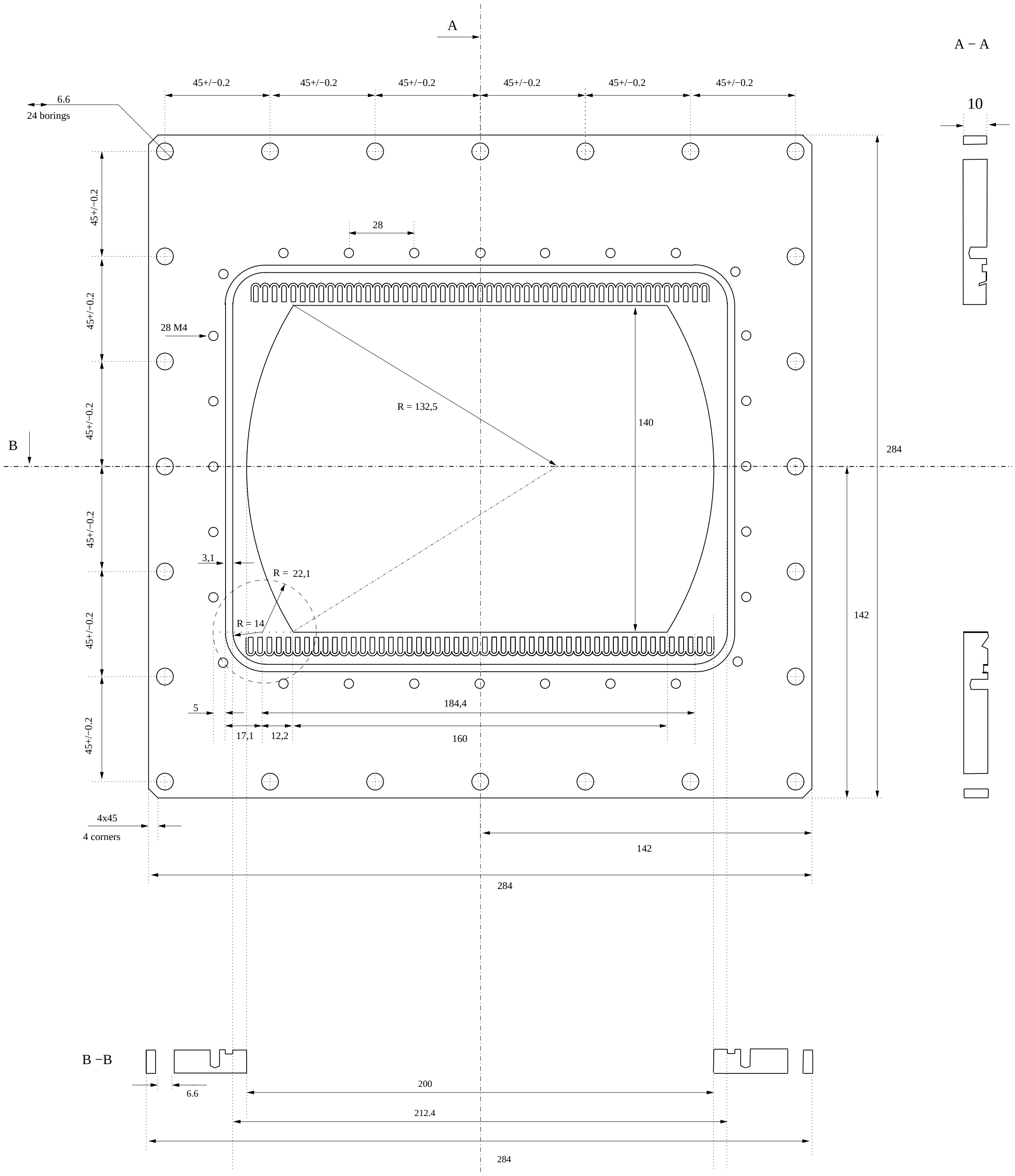

Figure A.3: Front view of the detector window

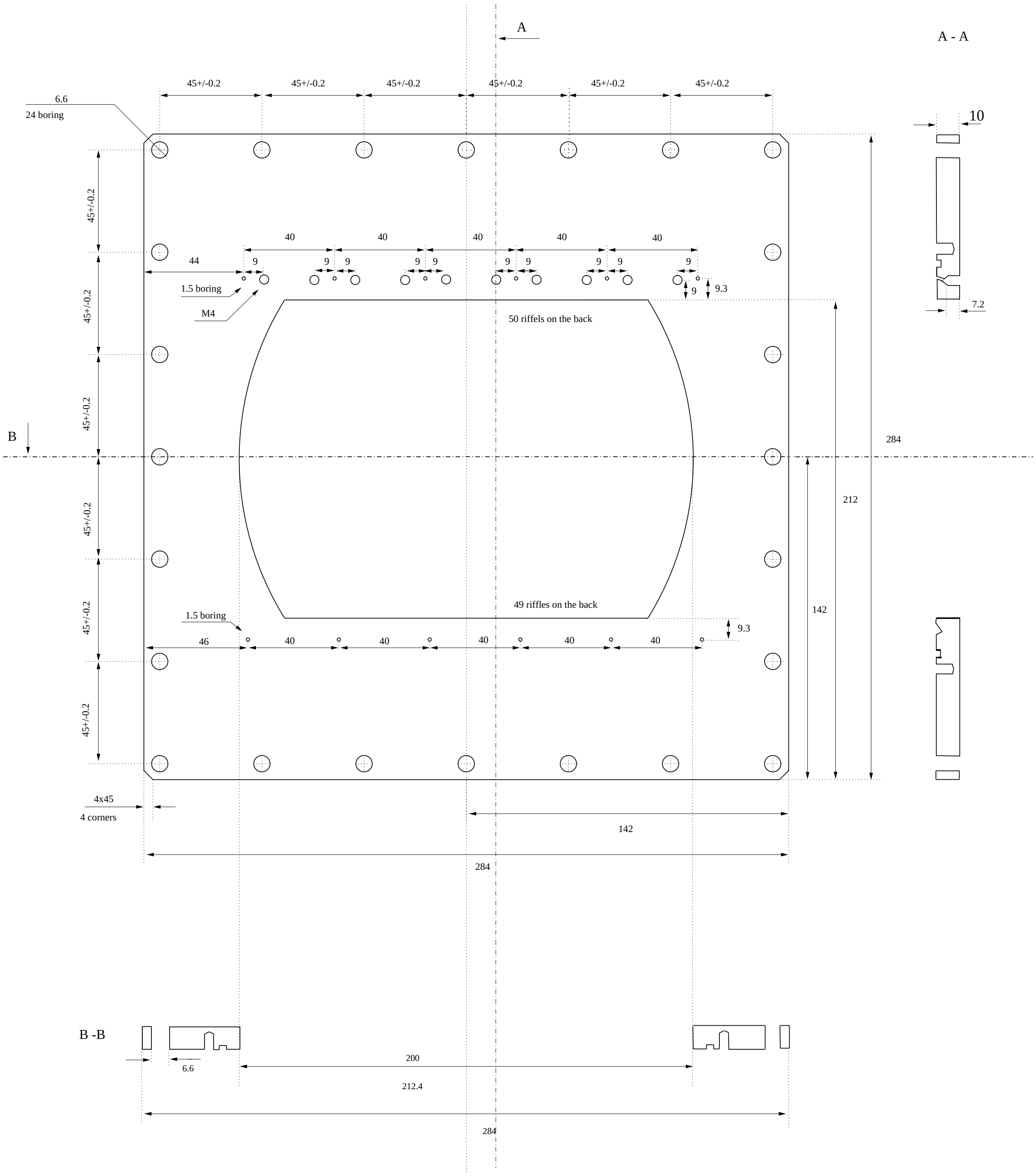

Figure A.4: Back view of the detector window

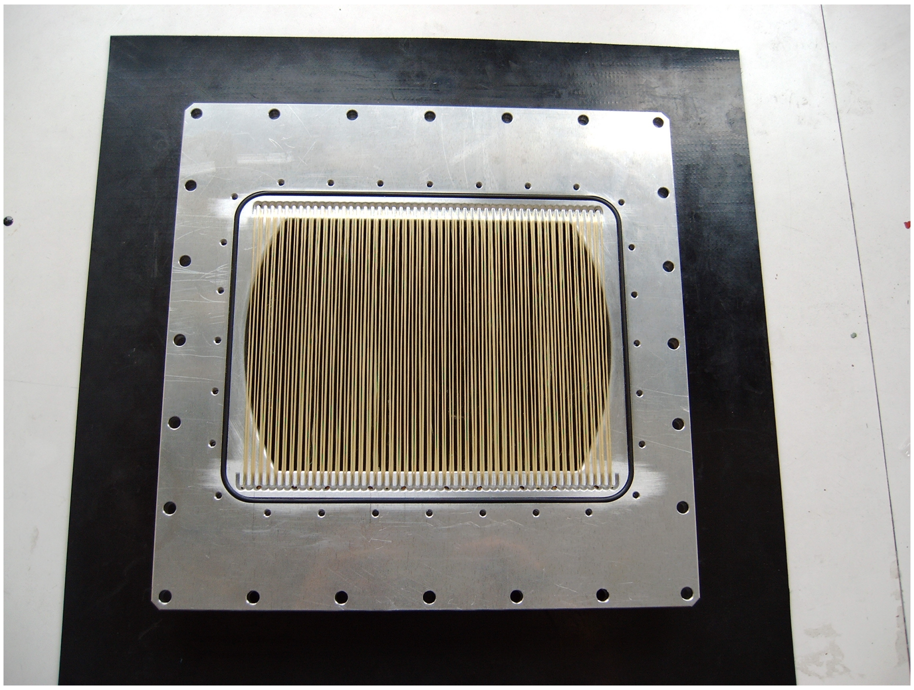

Figure A.5: Kevlar support construction with maximum mesh density of five yarn per centimeter of the detector window

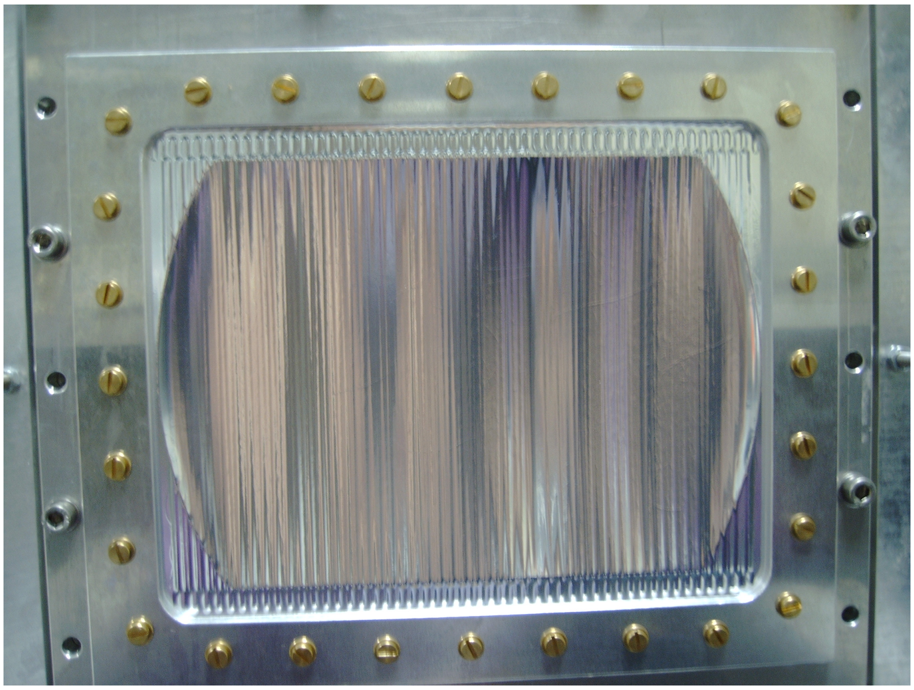

Figure A.6: Detector window mounted on the cryostat. The bulge of the window due to the vacuum, the Kevlar mesh structure and the aluminum flange can be seen.

Appendix B

Experimental Setup of the Silicon Detectors in COMPASS 2003

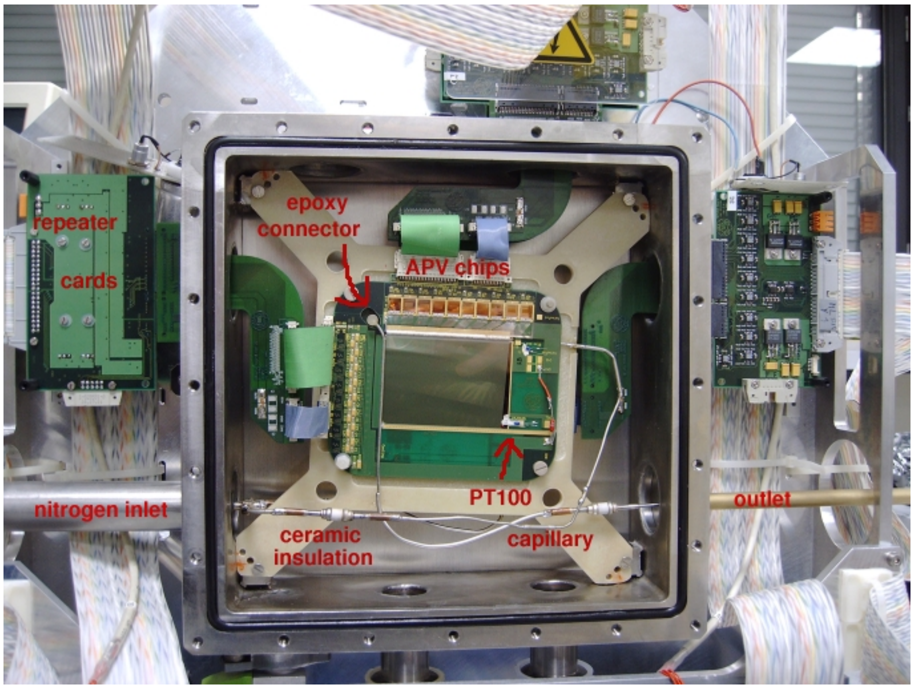

Figure B.1: The silicon detector glued on the L-boards mounted on a stesalit frame. The ten APV read out chips of one detector side are connected to the repeater cards via vacuum feedthroughs (flange flies). The infrastructure for the nitrogen supply can seen as well as the PT100 for temperature measurement placed on the silicon detector

Figure B.2: On top of the concrete block the blue optical bench with its granite precision rail can be seen to which the cryostats of the three silicon stations are mounted each housed in an aluminum frame. On the left the black covered veto detectors in front of the scintillating fiber station.

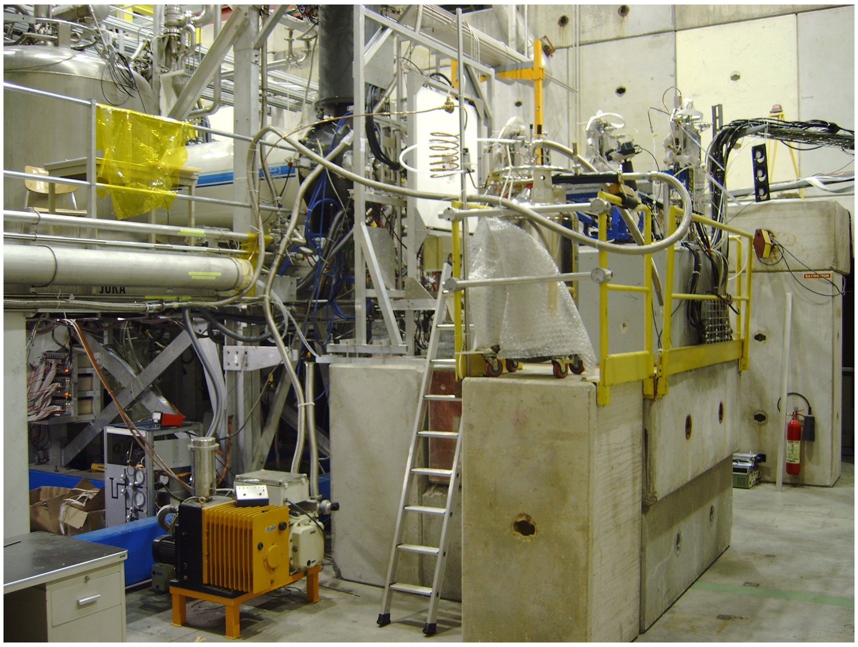

Figure B.3: This picture shows the transfer-line for refilling the self-pressurizing dewar, which is standing on top of the concrete block. In the background one sees the three silicon stations on the blue frame. Further the second scintillating fiber station and the target cylinder are visible on the right.

Appendix C

Occupancies

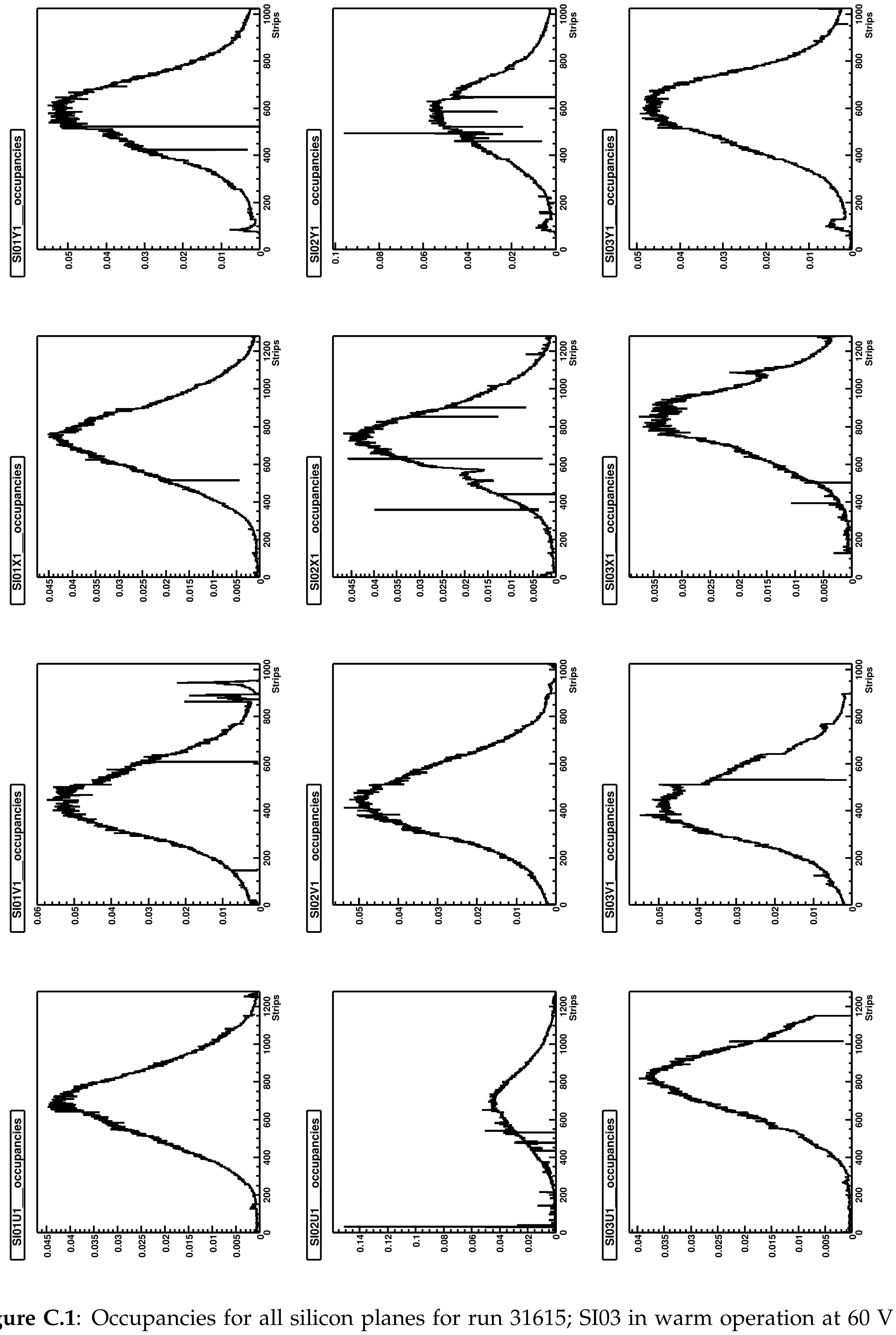

Figure C.1: Occupancies for all silicon planes for run 31615; SI03 in warm operation at 60 V in U/V and 50 V in X/Y

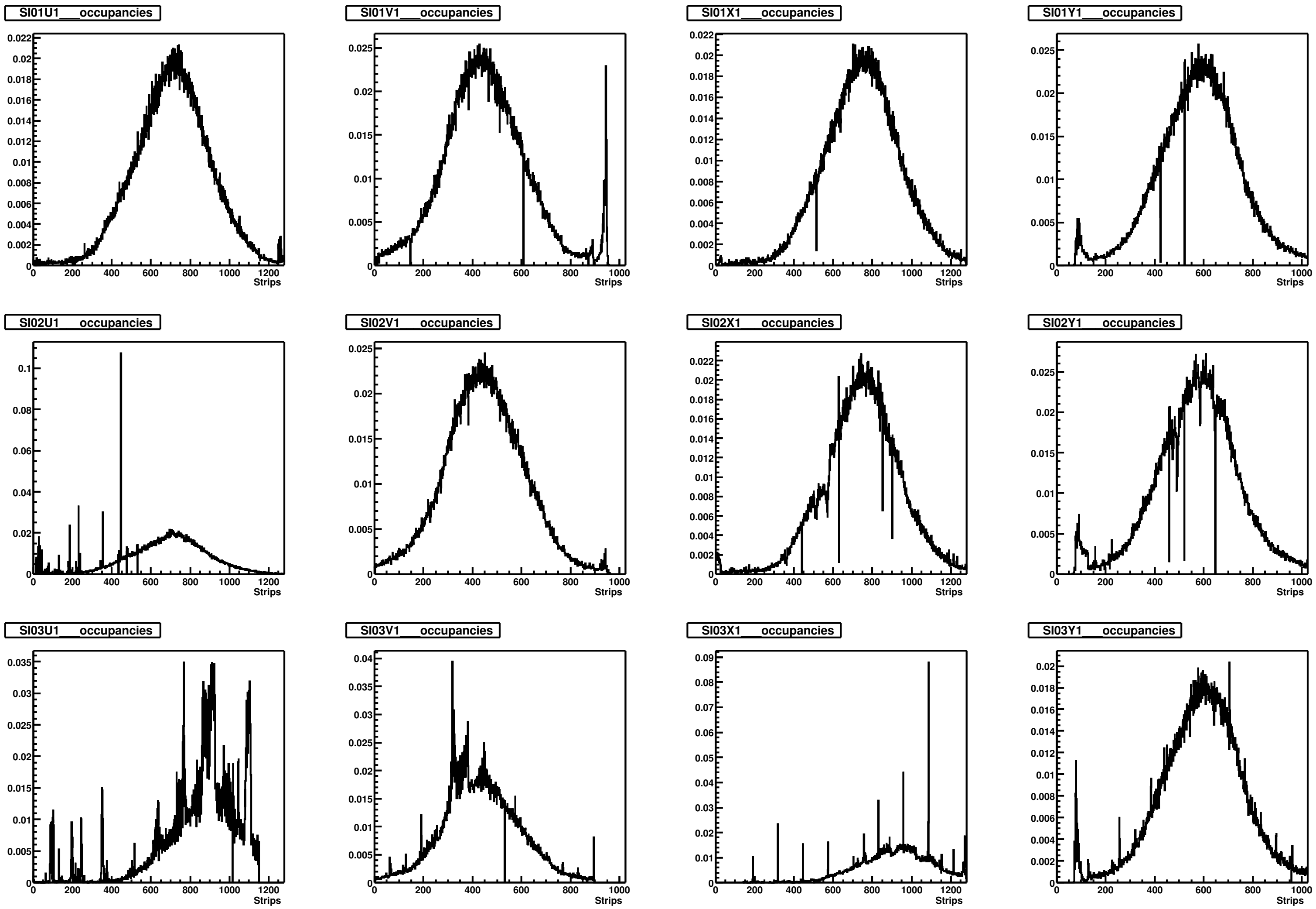

Figure C.2: Occupancies for all silicon planes for run 32454, SI03 in cryogenic operation at 60 V in U/V and 50 V in X/Y

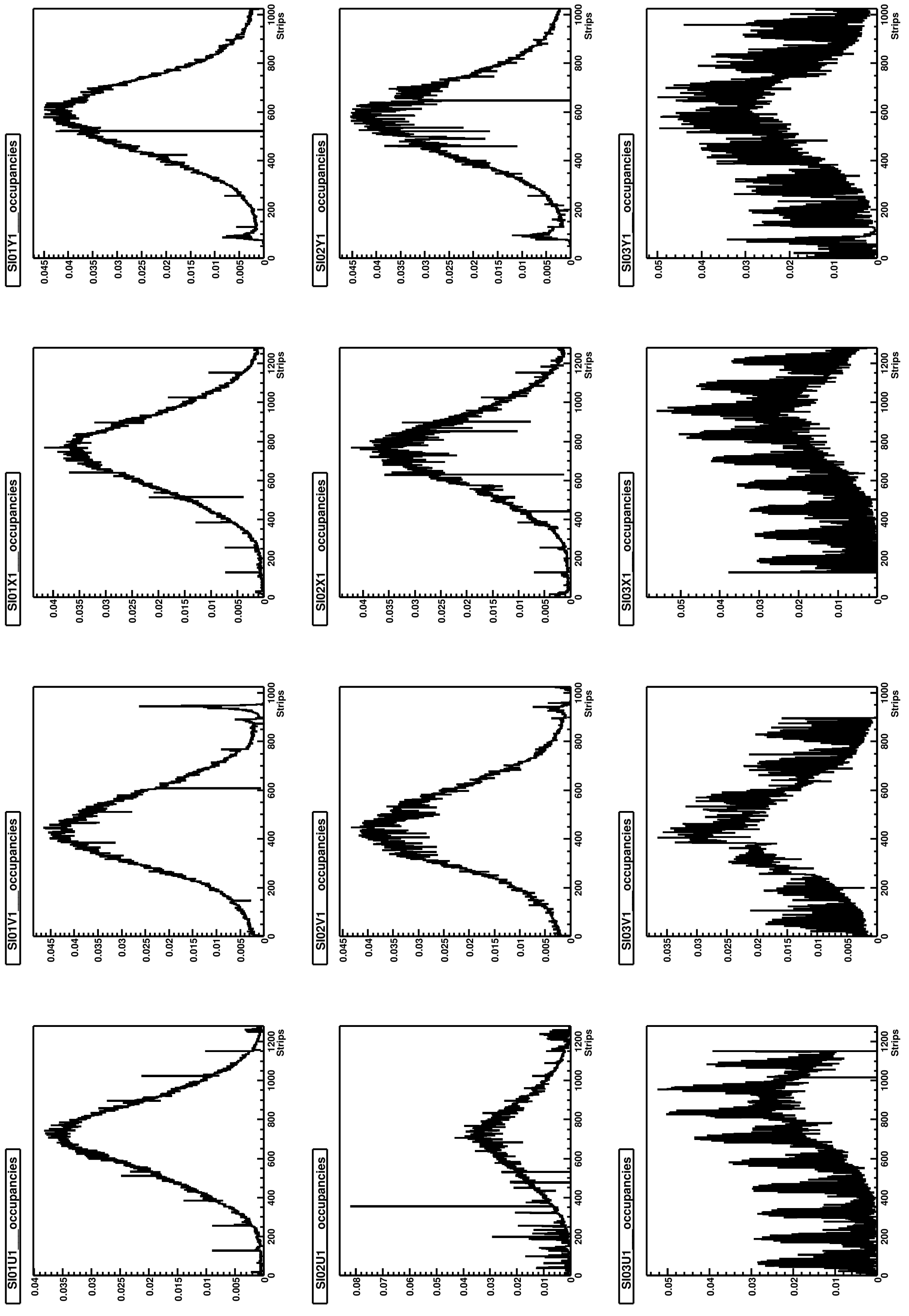

Figure C.3: Occupancies for all silicon planes for run 32496, SI03 in cryogenic operation at 40 V in U/V and 30 V in X/Y

Bibliography

[A$^+$03] H. Angerer et al. Present status of silicon detectors in compass. *Nucl. Instrum. Meth.* **A512**, 229–238 (2003).

[Abt99] I. Abt et al. Double sided microstrip detectors for the high radiation environment in the HERA-B experiment. *MPI-PhE* **99-05** (1999).

[Bij01] E. van der Bij. CERN S-LINK homepage, `http://hsi.web.cern.ch/HSI/s-link/`.

[Bor00] K. Borer et al. Charge collection efficiency of irradiated Silicon detector operated at cryogenic temperatures. *Nucl. Instr. and Meth. in Phys. Res.* **A 440**, 5–16 (2000).

[CO96] The COMPASS collaboration. A proposal for a Common Muon and Proton Apparatus for Structure and Spectroscopy. *CERN* **SPSLC 96-14** (1996).

[Gat00] L. Gatignon. The modifications to the M2 beam for COMPASS, `http://sl.web.cern.ch/SL/eagroup/NewM2/main.html`.

[Gat01] L. Gatignon. User guide for the M2 beam, `http://gatignon.home.cern.ch/gatignon/M2manual.html`.

[Gru01] B. Grube. *The trigger control system and the common GEM and Silicon readout for the COMPASS experiment*. Diploma thesis, TU München, December 2001.

[Ket01] B. Ketzer. `gemMonitor`, Online analysis tool for GEM and Silicon detectors. (2001).

[KEV] Du pont wep page, `http://www.dupont.com/kevlar`.

[Leo94] W. R. Leo. *Techniques for Nuclear and Particle Physics Experiments*. Springer, 1994.

[Mol99] M. Moll. *Radiation Damage in Silicon Particle Detectors;microscopic defects andand macroscopic properties*. Ph. D. thesis, Universität Hamburg, (1999).

[Nie00] M. Niebuhr. *Entwicklung eines 250 MHz-Zhlers mit totzeitfreier Auslese fr das COMPASS-Experiment*. Diploma thesis, Universität Freiburg, November 2000.

[Pal98] V. Palmieri et al. Evidence for charge collection efficiency recovery in heavily irradiated Silicon detectors operated at cryogenic temperatures. *Nucl. Instr. and Meth. in Phys. Res.* **A 413**, 475–478 (1998).

[PDG00] D. E. Groom et al. Review of particle physics. *European Physical Journal C* **15**, 1–878 (2000).

[Pei92] A. Peisert. Silicon microstrip detectors. *Adv. Ser. Direct. High Energy Phys.* **9**, 1–79 (1992).

[RD302] Rd39 status report 2001. (2002).

[Sau95] P. Sauer. *Entwicklung, Aufbau und Inbetriebnahme der vertikalen Driftkammern der Drei-Spektrometer-Anlage am Mainzer Mikrotron MAMI und Studium der Reaktion $^{12}C(e,e'p)^{11}B$ für mittlere und hohe Nukleonenimpulse im Kern*. Ph. D. thesis, Johannes Gutenberg Universität Mainz, Mai 1995.

[W^{+}95] W.Press et al. *Numerical Recipies in C*. Cambridge University Press, 1995.

[Wag01] R. Wagner. *Commissioning of Silicon Detectors for the COMPASS Experiment at CERN*. Diploma thesis, TU München, December 2001.

[Wie03] M. Wiesmann. *?* Phd thesis in preparation, TU München, (2003).

Own contributions

This thesis has been done within the framework of the chair of Prof. Paul at the Technical University of Munich and at the COMPASS collaboration at CERN, Geneva.

During the first part of this thesis together with Heinz Angerer I developed the electrical connections and relay circuit for the motor of the control valve for the liquid nitrogen distribution. This will be installed for the next beamtime. I also worked out a safety concept in teamwork together with Igor Konorov, Heinz Angerer and Christian Hoeppner of the control system for a silicon station in cryogenic operation which is realized in a separate safety control system, which is ready to be installed next year.

Most of the time was spent in developing a low mass, vacuum and light tight detector window for the silicon station. Several technical drawings, calculations, tests of single components, manufacturing of the Kevlar mesh and organizing light tight mylar foil were done. On this point I would like to thank Wolfgang Schott for his great advise to abandon the concept of a bended holding structure and to clamp the foil instead of gluing it onto the flange. After successful working prototype window, four additional windows were manufactured and used at CERN. Further tests were done to figure out if the mass density of the detector window can be reduced. Thanks to Steffi Grabmüller for her continuous help throughout the test and manufacturing phase.

For the COMPASS beamtime 2003, I was involved in the hardware installation, cabling and commissioning of the two official COMPASS silicon detectors in April 2003. Together with Rita de Masi a complete test setup of a silicon station cooled with liquid nitrogen was installed in the laboratory. A lot of time was spent in searching for reasons of the vacuum leaks. Due to time constraints only the functionality could be proven but no detailed determination of the detector properties.

The third silicon station was installed at CERN in the beginning of June, but only prepared for warm operation. I installed a nitrogen gas cooling system for this station like it is already realized for the other two stations. The cooling facilities were brought and installed at CERN step by step during the machine developments. First cooling tests were done end of July. After the regular COMPASS physics run, detector test were possible during the 25ns run. There, I took responsibility on the commissioning of the silicon station in cryogenic operation and taking data. These data are basis for the analysis. In order to obtain the spatial resolution of the silicon detectors I spent much time in calibrating the particular runs. First results of the analysis on a silicon detector in warm and cold operation are presented within this thesis.

Acknowledgements

First I would like to thank Prof. Stephan Paul for giving me the chance to work on the cryogenic setup for a cooled silicon station and to learn how much work is necessary and how many details have to be considered to get a low temperature detector running. Apart from that the several trips to CERN gave insight in the fascinating world of high energy particle physics.

I am deeply grateful to Jan Friedrich, for a lot of support, ideas concerning the development of the detector window and the introduction in the detector analysis. He showed a lot of patience in teaching me C++ and how to work with ROOT. I really learned a lot from him and without his continuous advice this thesis would not have been possible.

Special thanks to Rita de Masi for the introduction in cryogenic operated silicon station and for the effective installation times at CERN.

Also Boris Grube deserves many thanks for his kind help by all kinds of computer problems and Roland Kuhn as well, especially for for writing some scripts and allowing me to use his TEX style file.

Further I am much obliged to the whole COMPASS group of their support and help, I really enjoyed to be a member of them.

Thanks to Jan, Boris, Elke, Matthias, Horst and Rita for proof-reading this manuscript and for figuring out the most important bugs.

Ganz besonders möchte ich mich bei meinen Eltern bedanken, die mich auf liebevolle Weise unterstützt und gefördert haben, meinen Weg zur Physik zu finden.

Herzlichster Dank geht an meinem Verlobten Horst Dinkelbach der mich nicht nur das letzte Jahr in vielerlei Hinsicht tatkrätfig unterstützt hat.

Mein Zimmerdschungel bedankt sich bei Elke und Elfi, dass er während meiner Abwesenheit am CERN am Leben erhalten wurde.

Special thanks to Santa Claus for his present.